











# NAVAL POSTGRADUATE SCHOOL

## Monterey, California



## THESIS

Process-Dependence of Properties in  
High Thermal Conductivity  
Aluminum Nitride Substrates for Electronic Packaging

by

John H. Cooper

December, 1991

Thesis Advisor:  
Co-Advisor:

Indranath Dutta  
Shantanu Mitra

Approved for public release; distribution is unlimited

T259736



## REPORT DOCUMENTATION PAGE

1a REPORT SECURITY CLASSIFICATION UNCLASSIFIED			1b RESTRICTIVE MARKINGS	
2a SECURITY CLASSIFICATION AUTHORITY			3 DISTRIBUTION/AVAILABILITY OF REPORT Approved for public release; distribution is unlimited.	
2b DECLASSIFICATION/DOWNGRADING SCHEDULE				
4 PERFORMING ORGANIZATION REPORT NUMBER(S)			5 MONITORING ORGANIZATION REPORT NUMBER(S)	
6a NAME OF PERFORMING ORGANIZATION Naval Postgraduate School		6b OFFICE SYMBOL (If applicable) 034	7a NAME OF MONITORING ORGANIZATION Naval Postgraduate School	
6c ADDRESS (City, State, and ZIP Code) Monterey, CA 93943-5000			7b ADDRESS (City, State, and ZIP Code) Monterey, CA 93943-5000	
8a NAME OF FUNDING/SPONSORING ORGANIZATION		8b OFFICE SYMBOL (If applicable)	9 PROCUREMENT INSTRUMENT IDENTIFICATION NUMBER	
8c ADDRESS (City, State, and ZIP Code)			10 SOURCE OF FUNDING NUMBERS	
			Program Element No	Project No
			Task No	Work Unit Accession Number
11 TITLE (Include Security Classification) Process-Dependence of Properties in High Thermal Conductivity Aluminum Nitride Substrates for Electronic Packaging				
12. PERSONAL AUTHOR(S) John H. Cooper, LT, USN				
13a TYPE OF REPORT Master's Thesis		13b TIME COVERED From To		14 DATE OF REPORT (year, month, day) December, 1991
				15 PAGE COUNT 91
16 SUPPLEMENTARY NOTATION The views expressed in this thesis are those of the author and do not reflect the official policy or position of the Department of Defense or the U.S. Government.				
17 COSATI CODES			18 SUBJECT TERMS (continue on reverse if necessary and identify by block number)	
FIELD	GROUP	SUBGROUP	aluminum nitride, microelectronic packaging, liquid phase sintering, ceramic, yttria dopant, thermal conductivity	
19 ABSTRACT (continue on reverse if necessary and identify by block number) The development of secondary phases due to the presence of $Y_2O_3$ additions during sintering of aluminum nitride was studied. Depending on the amount of $Y_2O_3$ added, two non-equilibrium phases (cubic $YAlO_3$ and orthorhombic $AlYO_3$ ) were found to be present at room temperature, in addition to equilibrium $Al_5Y_3O_{12}$ and $Al_2Y_4O_9$ . Sintering at increasing temperatures was found to alter the proportions of the above phases. This appreciably affected physical properties and mechanical properties like density, stiffness, strain to fracture, and failure morphology. These changes were rationalized on the basis of the microstructural effects of sintering. TEM studies were also conducted to investigate the evolution of bulk and surface defects in sintered AlN during processing. In the low $Y_2O_3$ containing samples, heat treatment at 1850C resulted in a two phase mixture of Y-aluminate, and gamma- $Al_2O_3$ at the triple grain boundaries in AlN. Based on these results, a mechanism for the sintering process is proposed.				
20 DISTRIBUTION/AVAILABILITY OF ABSTRACT <input checked="" type="checkbox"/> UNCLASSIFIED/UNLIMITED <input type="checkbox"/> SAME AS REPORT <input type="checkbox"/> DTIC USERS			21. ABSTRACT SECURITY CLASSIFICATION UNCLASSIFIED	
22a NAME OF RESPONSIBLE INDIVIDUAL Indranath Dutta, Professor			22b TELEPHONE (Include Area code) (408) 646-2581	
			22c OFFICE SYMBOL 69DU1	

Approved for public release; distribution is unlimited.

Process-Dependence of Properties in  
High Thermal Conductivity Aluminum Nitride Substrates for  
Electronic Packaging

by

John H. Cooper  
Lieutenant, United States Navy  
B.S., Pennsylvania State University

Submitted in partial fulfillment  
of the requirements for the degree of

MASTER OF SCIENCE IN MECHANICAL ENGINEERING

from the

NAVAL POSTGRADUATE SCHOOL

December 1991

Anthony J. Healey, Chairman  
Department of Mechanical Engineering



## ABSTRACT

The development of secondary phases due to the presence of  $Y_2O_3$  additions during sintering of Aluminum Nitride was studied. Depending on the amount of  $Y_2O_3$  added, two non-equilibrium phases (cubic  $YAlO_3$  and orthorhombic  $AlYO_3$ ) were found to be present at room temperature, in addition to equilibrium  $Al_5Y_3O_{12}$  and  $Al_2Y_4O_9$ . Sintering at increasing temperatures was found to alter the proportions of the above phases. This appreciably affected physical properties and mechanical properties like density, stiffness, strain to fracture, and failure morphology. These changes were rationalized on the basis of the microstructural effects of sintering. TEM studies were also conducted to investigate the evolution of bulk and surface defects in sintered AlN during processing. In the low  $Y_2O_3$  containing samples, heat treatment at  $1850^\circ C$  resulted in a 2 phase mixture of Y-aluminate and  $\gamma-Al_2O_3$  at the triple grain boundaries in AlN. Based on these results, a mechanism for the sintering process is proposed.

120315  
C 754043  
C.1

## TABLE OF CONTENTS

I. INTRODUCTION . . . . .	1
A. PROPERTIES OF ALUMINUM NITRIDE (AlN) . . . . .	1
B. SINTERING OF AlN POWDERS . . . . .	4
C. PROPERTIES OF SINTERED AlN . . . . .	9
D. DEFECTS IN SINTERED AlN . . . . .	12
E. OBJECTIVES OF THE PRESENT STUDY . . . . .	15
II. EXPERIMENTAL . . . . .	17
A. HEAT TREATMENT . . . . .	17
B. X-RAY DIFFRACTION . . . . .	18
C. DENSITY MEASUREMENTS . . . . .	19
D. THREE-POINT BEND TESTING . . . . .	19
E. SCANNING ELECTRON MICROSCOPY (SEM) . . . . .	21
F. GRAIN SIZE DISTRIBUTION . . . . .	21
G. TRANSMISSION ELECTRON MICROSCOPY . . . . .	22
III. RESULTS AND DISCUSSION . . . . .	23
A. PROPERTIES OF AS-RECEIVED SAMPLES . . . . .	23

B. PHASE CONSTITUTION OF AS-RECEIVED AND HEAT TREATED AIN . . . . .	27
C. CHANGES IN MICROSTRUCTURE AND PROPERTIES WITH HEAT TREATMENT . . . . .	33
1. Scanning Electron Microscope (SEM) Study . . . . .	33
2. Grain Size Distribution . . . . .	38
3. Density Changes Due to Sintering . . . . .	41
4. Mechanical Properties . . . . .	43
5. Transmission Electron Microscope Study . . . . .	52
IV. CONCLUDING REMARKS . . . . .	76
LIST OF REFERENCES . . . . .	80
INITIAL DISTRIBUTION LIST . . . . .	83





## I. INTRODUCTION

### A. PROPERTIES OF ALUMINUM NITRIDE (AlN)

Recent advances in high performance electronic devices, such as high speed VLSI's, logic circuits, and high power transistors have produced devices with a higher circuit density that produce a large amount of heat. This has led to a search for substrate materials offering high thermal conductivity as well as good electrical resistivity [Ref.1-7].

$\text{Al}_2\text{O}_3$  is currently the most commonly used substrate material in microelectronic packaging. However, its low thermal conductivity and high coefficient of expansion have led researchers to investigate other materials. AlN, BeO, and SiC (doped with BeO) have been suggested as candidates [Ref.1,2]. Table 1 compares the some of the properties of current substrate candidates with silicon.

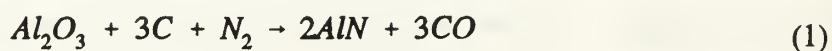
The properties of AlN substrate material compare well with those of the other substrate materials. In addition to a thermal conductivity up to ten times that of  $\text{Al}_2\text{O}_3$ , AlN has a coefficient of thermal expansion that is closer to that of silicon. BeO has an higher thermal conductivity than AlN, however its coefficient of thermal expansion is significantly higher than that of silicon, and its high toxicity creates handling problems during manufacture that lead to high production costs. SiC possesses a higher thermal conductivity than AlN, but doping with BeO adds toxicity and results in a dramatic drop in dielectric strength. Thus the combination of high thermal conductivity, high dielectric

strength, and low thermal expansion combine to make AlN a very attractive substrate material worth further investigation.

**Table 1**  
**Properties of Electronic Ceramic Substrates With Silicon [Ref.2]**

	AlN	Al <sub>2</sub> O <sub>3</sub>	BeO	SiC (BeO)	Si
Thermal Conductivity W/mK	160 to 250	25	260	270	150
Coefficient of Thermal Expansion (*E <sup>-6</sup> /°C)					
(20 to 100°C)	2.65	7	6.5	3.7	2.3
(20 to 400°C)	4.8	7.4	8.0	3.7	-
Dielectric Strength (20°C)(kV/mm)	14-17	10-15	10-14	0.07	-
Bending Modulus (GPa)	331	338	324	393	165
Density (g/cm <sup>3</sup> )	3.26	3.75	2.9	3.2	2.3

Commercial AlN powders are commonly synthesized via two methods: carbothermal reduction of Al<sub>2</sub>O<sub>3</sub>, and direct nitridation of aluminum metal. Other methods of AlN synthesis include reaction of AlF<sub>3</sub> with ammonia, and the decomposition of organometallics [Ref. 2]. Carbothermal reduction methods utilize the following reaction:





Although  $\text{Al}_2\text{O}_3$  is very stable, even at elevated temperatures, this reaction proceeds at around  $1600^\circ\text{C}$  due to the high free energy of formation of CO [Ref.2].

Direct nitridation of aluminum follows the equation:



This reaction is typically carried out below  $1400^\circ\text{C}$ . Oxygen partial pressure is extremely important due the competing reaction of aluminum oxidation [Ref.2]:



Slack and McNelly [Ref. 8], have developed a method to make high purity single crystals of AlN. Nitriding of aluminum takes place in a "pellet drop" technique which involves dropping cylindrical aluminum pellets into a heated crucible within a 95 %  $\text{N}_2$  + 5 %  $\text{H}_2$  atmosphere. The molten aluminum reacts with the nitrogen to produce AlN. The boron nitride crucible is heated by radio frequency energy, and is the only material the molten aluminum comes into contact with. Single crystals are grown in a tungsten tube furnace that rotates the specimen while pulling it through the hot zone. The resultant single crystal of AlN is amber in color, and has a measured thermal conductivity of 250 W/mK; 78% of the theoretical value of 320 W/mK as predicted by Slack in earlier work [Ref.9]. This result has become an important standard for polycrystalline AlN comparison.

AlN substrates are manufactured by different means. The most common is that of tape casting. In this method the powder is mixed with appropriate binder, solvent and plasticizer. This slurry is spread onto a flexible backing (usually a plastic sheet), with a doctor blade. After the solvent has been removed, the resulting "tape" of material is removed from the backing. This produces a flexible thin uniform sheet for further processing into a substrate, which may include laminating with other green sheets, sintering, and metalization. This method has the advantage that fairly large and thin substrates can be mass produced at low cost [Ref.7].

Other forming methods include uniaxial pressing, then sintering, hot pressing, and hot isostatic pressing. The first two methods are limited to producing simple shapes, that will often require subsequent machining for substrate use. In isostatic pressing, a green compact is made by pressing the powder and binder mixture in a die much like forming a pill. The green compact must then be removed from the die, and fired in a furnace to remove the binder, then to sinter the material. In hot pressing, the furnace is built around the die, so sintering takes place under uniaxial pressure. This pressure aids in the densification of the ceramic. In hot isostatic pressing (HIP), the sample is formed, then sealed and placed within a pressurized furnace. Because pressure is applied isostatically, complex forms can be produced, however, cost can be prohibitive.

## **B. SINTERING OF AlN POWDERS**

One facet of the research into AlN is the effect of sintering aids upon the densification and the behavior of these aids in the final product. Several sintering aids

have been investigated, focusing on calcium compounds and yttrium oxide [Ref.5,10,11,12]. The effect of these additives falls into two main categories. Firstly to scavenge oxygen from the AlN grains, and secondly to create a liquid phase to maximize densification through liquid phase sintering (LPS).

LPS has a profound effect upon the densification of a ceramic. Through LPS, densification can take place without the addition of external pressure during sintering [Ref.5,11]. Horvath, et. al., [Ref. 14] reports that the densification of undoped AlN can reach 95 % theoretical when sintered at high temperatures for extended periods of time. Further densification is limited by pore-grain boundary separation. Figure 1 shows an SEM micrograph of a relief polished surface of undoped AlN fired at 1930°C for 8 hours [Ref.14]. The micrograph reveals trapped pores within the grains limiting final density. The addition of a dopant, which forms a liquid phase at sintering temperatures, makes a profound difference. Figure 2 [Ref.14], shows a plot of relative density versus sintering time for undoped AlN, and AlN doped with CaO. The addition of just 2 wt% CaO resulted in a higher relative density, in a much shorter period of time.

LPS proceeds in three steps. First the grains are rearranged by sliding over one another to improve packing, and eliminate voids between the particles. This rearrangement is brought about under the action of capillary pressure by collapse of fluid bridges between particles. Concurrently, the liquid phase is distributed along the grain boundaries, concentrating at the triple-grain junctions. The second stage of LPS is a solution-reprecipitation or accommodation stage often called "Ostwald ripening." In this stage material is transported from high energy regions, (regions of sharper radius of





**Figure 1:** SEM micrograph of undoped AlN sintered at 1930°C for 8 hours showing pores trapped within the AlN grains limiting final density [Ref.14].

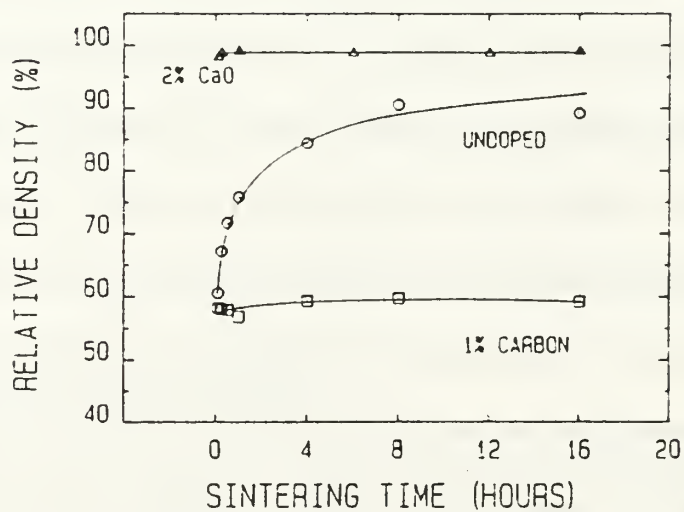


**Figure 2:** Relative Density vs. Sintering Time for AlN, showing dramatic increase in density at shorter times with dopant [Ref.14]

curvature), on the grain surface to lower energy regions. As the material is reprecipitated, rounding of the grain corners is observed. In the final, or third stage of LPS, the liquid phase is concentrated solely at the triple grain junctions, allowing the grains to come into contact with each other which leads to solid state sintering [Ref.15]. Figure 3 shows a typical LPS microstructure [Ref.15].

The primary impurity in AlN powder exists in the form of  $\text{Al}_2\text{O}_3$  on the surface of the AlN powders, and as dissolved oxygen in the AlN lattice. The addition of CaO to AlN has been found to form a calcium aluminate phase at the grain boundaries that appears to draw oxygen from the AlN grains. This phase is reported to evaporate from the material with extended heat treatment [Ref.10,14]. The addition of carbon to AlN, (in the form of  $\text{CaC}_2$  or carbon black), also reduced the amount of oxygen present, possibly as CO or  $\text{CO}_2$  gas [Ref.10]. Carbon however had a negative influence on densification when added alone, and has been found to inhibit grain growth [Ref.2,12,14].

The addition of  $\text{Y}_2\text{O}_3$  has also been found to maximize densification and reduce oxygen content within the AlN grains. Oxygen is thought to be removed from the grains in a two stage process. Dissolved oxygen in AlN is believed to be drawn to the grain boundary during sintering. At the grain boundary, this oxygen, along with the  $\text{Al}_2\text{O}_3$  film on the AlN powder particles, reacts with  $\text{Y}_2\text{O}_3$  to form yttrium aluminate phases with yttria to alumina ratios of 1:1, 1:2, and 3:5, i.e.  $\text{AlYO}_3$ ,  $\text{Al}_2\text{Y}_4\text{O}_9$ , and  $\text{Al}_3\text{Y}_5\text{O}_{12}$ , [Ref.2]. The yttrium-aluminate phases form a liquid phase during sintering to promote densification through LPS. The yttrium-aluminate phases are found on the grain

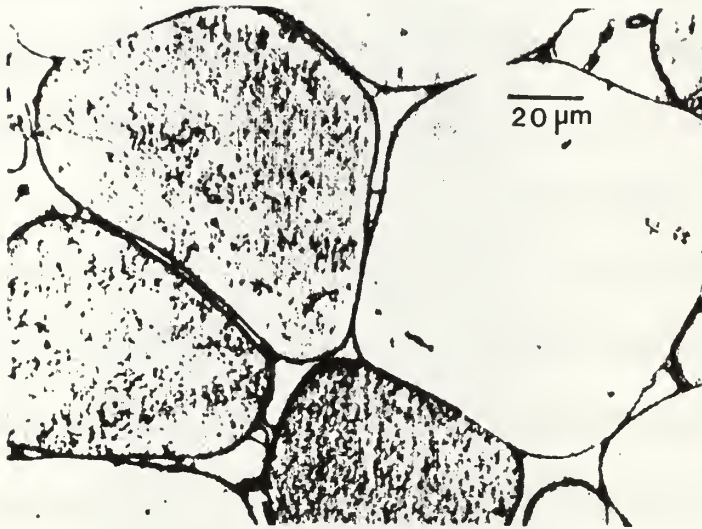


Figure 3: SEM micrograph of typical LPS microstructure [Ref.15]

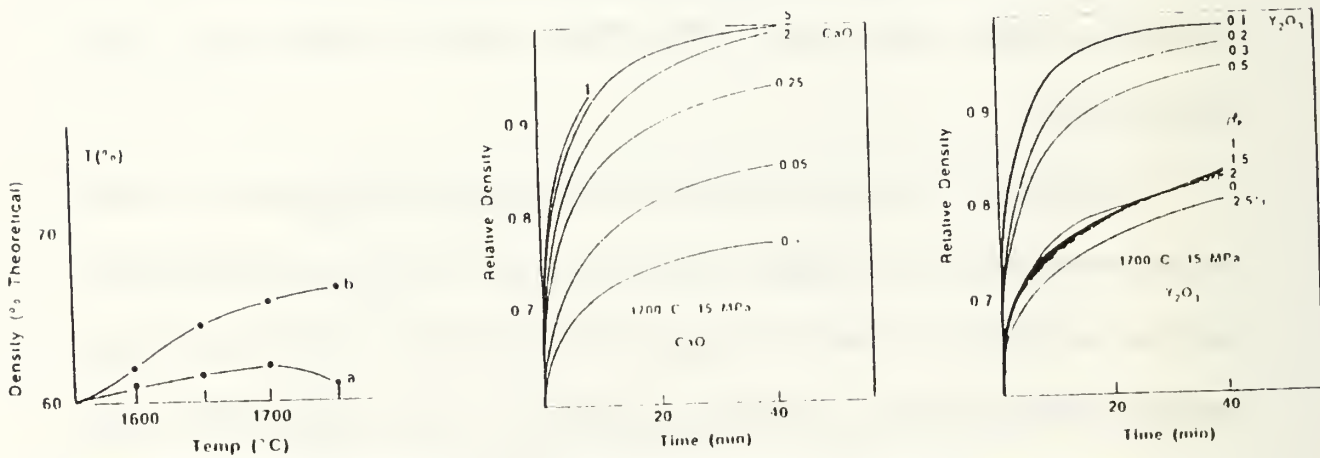


Figure 4: Densification of AlN dopant free, with CaO, and with Y<sub>2</sub>O<sub>3</sub>, showing greater density, and shorter time required for densification with dopants [Ref.17]



boundaries, and at the triple grain junctions. Takahashi, et. al., [Ref.16], reported that the amount of  $Y_2O_3$  present after sintering was less than that added initially, indicating possible evaporation of the yttrium-aluminate phase.

### C. PROPERTIES OF SINTERED AlN

The properties of sintered AlN were presented in Table 1. There is significant variation however in these properties depending upon the dopants and heat treatment. Figures 4a, b, and c, [Ref.17], show the effects of dopants on density. Without any dopants, (Figure 4a), the maximum density reached as a function of temperature was 67% of theoretical ( $3270 \text{ kg/m}^3$ ). With the addition of CaO or  $Y_2O_3$ , (Figures 4b, and 4c), density reaches near theoretical in a short period of time, at a lower temperature. Thermal conductivity verses density data for undoped dry-pressed and sintered AlN, and for hot pressed AlN are presented in Figure 5, [Ref.12]. These report a maximum thermal conductivity of 75 W/mK for dry-pressed and sintered AlN, and 90 W/mK for hot pressed AlN at a higher density, indicating a direct connection between density and thermal conductivity. Figure 6, [Ref.12], shows the results of several studies of the effects of dopants on density and thermal conductivity of AlN. CaO and  $CaC_2$  dopants have been found to produce AlN with a thermal conductivity of 130-160 W/mK [Ref.12,14].  $Y_2O_3$  doped samples of AlN have been reported with thermal conductivity values of 150 to 260 W/mK [Ref.2].

The amount of dissolved oxygen present in the sintered material also has a direct connection to the final thermal conductivity. Figure 7 [Ref. 17,18], compares the

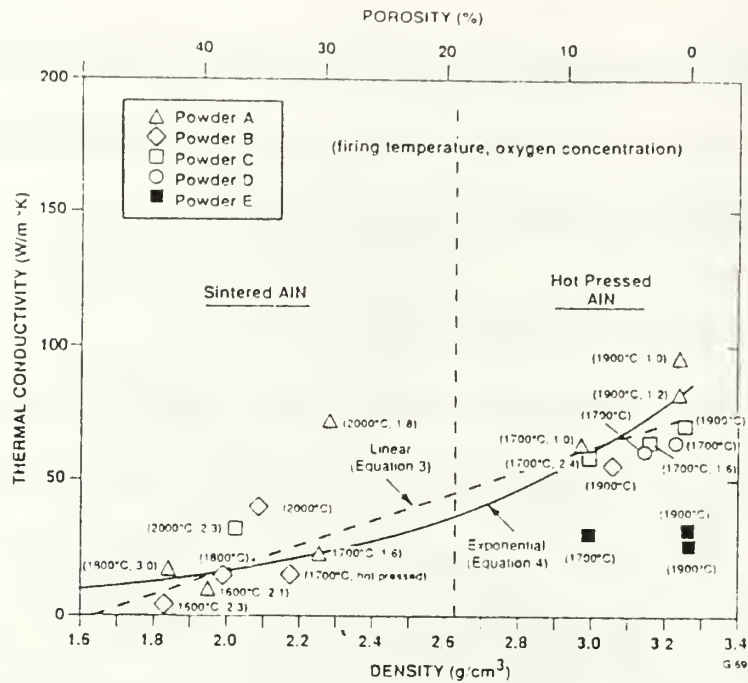


Figure 5: Thermal conductivity vs density data for sintered and hot-pressed undoped AlN [Ref.12]

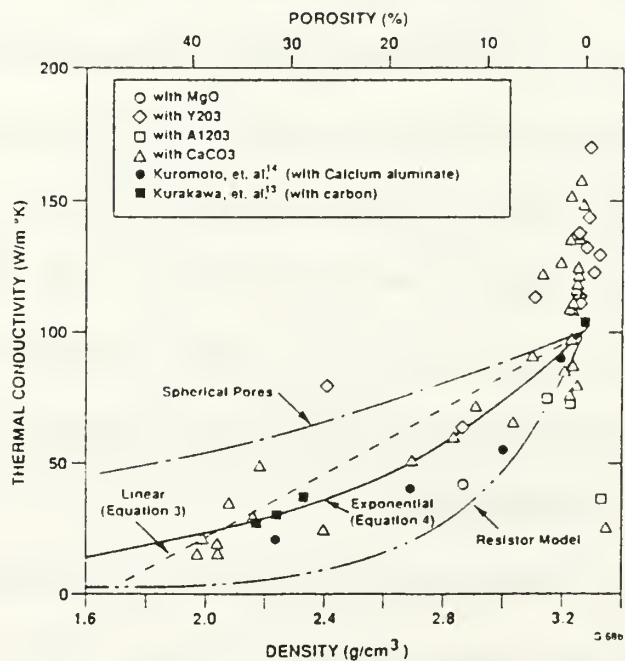
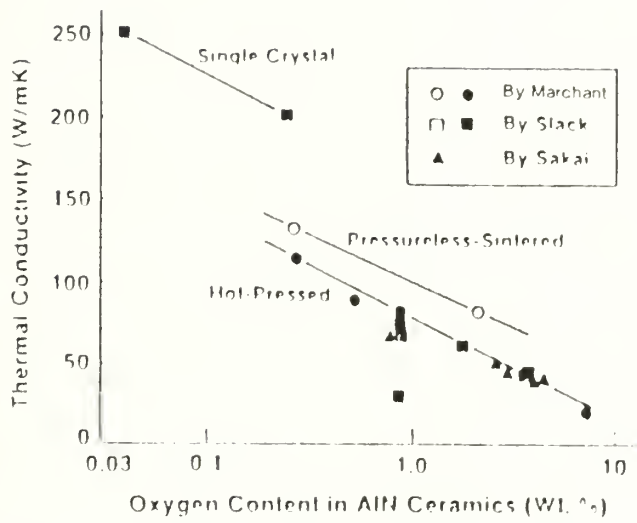


Figure 6: Density vs Thermal conductivity data, showing the effects of several dopants on AlN [Ref.12].



**Figure 7:** Thermal conductivity data of single crystal, hot pressed, pressureless sintered AlN (1 wt% CaO), as a function of oxygen content, showing decrease of thermal conductivity with an increase in oxygen [Ref. 17,18].

thermal conductivity of single crystal, pressureless sintering (CaO dopant), and hot pressed AlN (no dopant), as a function of oxygen content. The thermal conductivity was found to be inversely proportional to the logarithm of the oxygen content.

#### **D. DEFECTS IN SINTERED AlN**

The role of oxygen in the thermal conductivity of AlN is of great interest. Oxygen is thought to replace nitrogen in the AlN matrix. This results in the elimination of an aluminum atom as a vacancy for every three oxygen solute atoms, to maintain charge balance. Since electrical insulators conduct thermal energy in the form of phonons and lattice vibrations, thermal conductivity is degraded by the presence of foreign atoms or vacancies. Phonons are easily scattered by defects within the structure, particularly vacancies. Scattering at the defects is controlled by differences in density between the defect and the matrix, indicating the significant effect that a vacancy has on scattering phonons [Ref.13]. The thermal resistance  $W$  of a sample with defect concentration  $y$  is expected to follow the simple relationship:

$$W \propto y(1 - y)\Gamma \quad (4)$$

where  $\Gamma$  is the phonon scattering cross section for the defect [Ref.13].

Dissolved oxygen in the AlN lattice has been seen to concentrate on extended defects under certain conditions. Harris, et. al., [Ref.13], has proposed a defect-cluster model to account for observed features in the microstructure. The sequence of events in this model are illustrated schematically in Figure 8, [Ref.13]. The addition of three

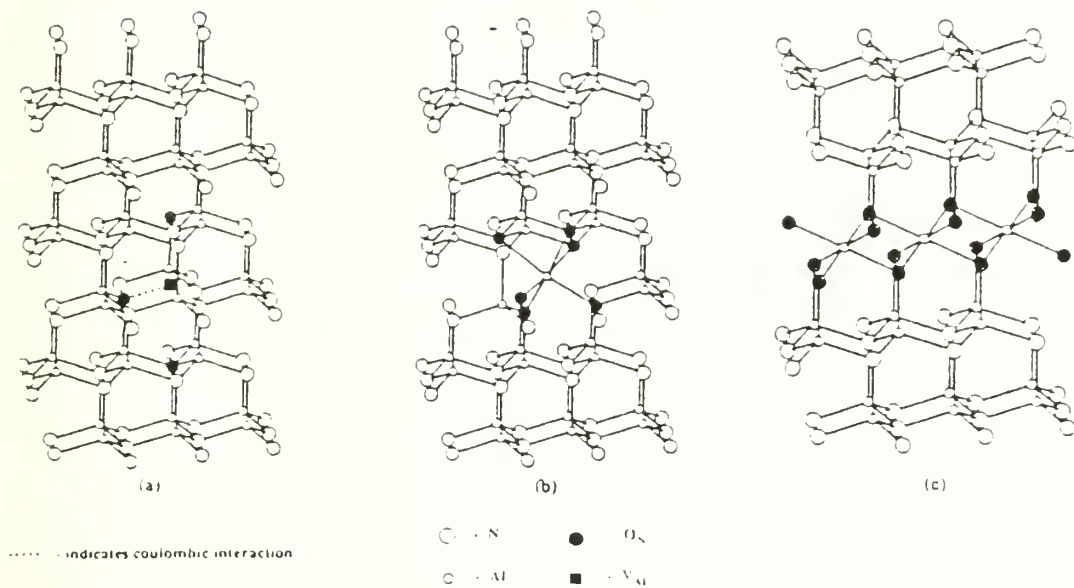


**Figure 8:** Schematic representation of Defect-Cluster model showing; (a) Local aluminum vacancy to maintain charge balance, (b) Annihilation of vacancy as aluminum bonds octahedrally with oxygen, (c) formation of extended defect [Ref.13].



oxygen atoms to the lattice is believed to produce one aluminum vacancy (Figure 8a). When the local oxygen concentration is increased above 0.75 %, the model predicts that the nature of the defect changes. As the oxygen concentration increases, the Al atoms are octahedrally bound to an increasing number of oxygen atoms. For each octahedral defect formed, two Al vacancies are annihilated. These create the localized defects in Figure 8b, and can be explain a decrease in unit cell volume with O content. As the oxygen content increases further, the octahedral defects organize to form extended defects such as an oxygen containing stacking fault, and an inversion domain boundary, (IDB), that is a special type of antiphase domain boundary which can only occur in crystals lacking a center of symmetry, (Figure 8c). This model is supported by changes in the oxygen related luminescence peak and the slope change of thermal conductivity with oxygen content at 0.75 %.

Investigations on the nature of IDBs in AlN confirm that oxygen has migrated from the grains to these regions [Ref.19,20]. The curved nature of the boundary is thought to be evidence of the non-stoichiometric nature of the IDB, i.e. either all Al-Al or N-N bonds, (and not alternating Al-Al, N-N bonds)[Ref.20]. Often these boundaries have precipitates or other defects associated with them [Ref.21].

When a planar IDB intersects with a curved IDB, a "D" shaped defect is formed. McKernan and Carter [Ref.22] have proposed a model for this defect with alumina lying on the planar IDB suggesting Al-O-Al bonds, while the curved IDB consists of N-N bonds, with no oxygen present. This was based upon contrast studies suggesting that the curved and planar faults bounding the "D" are different in nature, and that significant

oxygen is associated with the planar defect, but not the curved defect. This work is supported by Westwood and Notis [Ref.19] who found significantly less oxygen associated with curved IDBs than planar IDBs, and noted that fewer planar IDBs were found in samples doped with yttria to remove oxygen from the grains.

#### **E. OBJECTIVES OF THE PRESENT STUDY**

This study focuses on the microstructure and properties of AlN doped with  $Y_2O_3$ . No published work was found that studied the development of the yttrium aluminate phases during sintering and their effects on the properties of the sintered product. Consequently this study was undertaken to investigate:

- the development of the grain boundary yttrium-aluminate phases during heat treatment at temperatures between 1750°C and 1900°C
- the effect of the grain boundary phases on the mechanical properties of the sintered AlN
- the effect of different amounts of  $Y_2O_3$  on the grain boundary phase development during heat treatment and on the mechanical properties
- the effect of different manufacturing techniques on the microstructure and properties of AlN with equivalent amounts of sintering aids

- the correlation of the thermal conductivity with the changes in the microstructure observed after the various heat treatments

## II. EXPERIMENTAL

### A. HEAT TREATMENT

Three sets of samples were obtained from Keramont Advanced Ceramic Products Corporation, Tucson, AZ, and were labeled 7C, 7T, and 7R. The 7C and 7R samples were tape cast, while 7T was hot pressed. The 7R and 7T samples had approximately equal additions of  $Y_2O_3$  as a sintering aid, while the 7C sample had significantly less  $Y_2O_3$  added.

The heat treatment schedule utilized during this study is shown in Table 2. The as received samples were sectioned into 1.27 x 5.08 cm pieces. These samples were subjected to both varying times at the same temperature of 1850°C, and to varying temperatures at the same time of two hours. Only a single set of samples were prepared at the common two hour treatment at 1850°C. Heat treatment was carried out by CM Furnaces, Biddeford, Maine, in a continuous operation furnace. The atmosphere was controlled inside the furnace by maintaining a flow of dry nitrogen to prevent oxidation.

After heat treatment the samples were thoroughly cleaned to remove any contaminants deposited from the furnace chamber. This cleaning included grinding the surface with fine grit sand-paper to remove any contaminant layer from the surfaces.

The samples were sectioned with a diamond saw for preparation of electron microscope samples, X-ray diffraction samples, and density measurement samples.

**Table 2**  
**Heat Treatment Schedule**

<b>Sample/Heat Treatment</b>	<b>7C</b>	<b>7T</b>	<b>7R</b>
<b>T = 1850°C</b> <b>Varying Time</b>	<b>2 Hours</b>	<b>2 Hours</b>	<b>2 Hours</b>
	<b>7 Hours</b>	<b>7 Hours</b>	<b>7 Hours</b>
<b>T = 2 Hours</b> <b>Varying Temperatures</b>	<b>1750°C</b>	<b>1750°C</b>	<b>1750°C</b>
	<b>1800°C</b>	<b>1800°C</b>	<b>1800°C</b>
	<b>1850°C</b>	<b>1850°C</b>	<b>1850°C</b>
	<b>1900°C</b>	<b>1900°C</b>	<b>1900°C</b>

## **B. X-RAY DIFFRACTION**

A portion of each sample was chosen for X-Ray Diffraction (XRD). The samples were pulverized by mortar and pestle, then mounted on glass slides with amyl-acetate. Care was taken to ensure that a fine powder was produced, and that an even coating of the powder was present on the slide.

The samples were examined in a Phillips Systems goniometer controlled by a DEC VAX station. A scintillation counter is also attached to this station for processing the results. The scans were taken from 10° to 140° (two-theta) using steps of 0.05°, and



step times of two seconds. The 'd'-values were calculated using copper K $\alpha$  radiation, and used to index the patterns.

### C. DENSITY MEASUREMENTS

Density measurements were made on an analytical balance using Archimedes method. The mass of the samples was first determined in air. Then the samples were submerged in a fluid of known density, and the weight determined. The weight of the submerged sample holder was subtracted from the weight of the sample plus holder to determine the true weight of the sample. The density of the sample was then determined using the formula below. Three fluids were tested, and distilled water was found not to wet the surface of the samples well. Ethyl alcohol as well as distilled kerosene produced the best results.

$$\rho_{sample} = \frac{\rho_{liq} * mass\ dry}{mass\ dry - weight\ submerged} \quad (5)$$

### D. THREE-POINT BEND TESTING

Three-point bend testing was utilized to correlate the microstructure before and after heat treatment with the fracture properties and mechanical strength. In four-point testing, the sample will fail at the weakest point (where sintering is incomplete), since the sample within the inner two supports is primarily in tension. This does not give a representative fracture surface of the sintered product. In three-point testing the failure location is forced under the center support, not the weakest point in the sample.

The samples were cut into 0.381 x 5.08 cm sections and testing was accomplished on an electro-hydraulic Materials Testing System, Minneapolis, MN, model 810 electro-hydraulic test system equipped with a three-point bend fixture (model 642.05A-01), and displacement transducer (model 632.06B). The distance between the outer points in the fixture is 4.0 cm. An inverted ramping function was utilized to ramp the load from 0 to 100 lb<sub>f</sub> in 500 seconds. Data was collected with a Hewlett-Packard model 3852A data acquisition system which listed the force and displacement of the sample at discrete time intervals, as well as plotting force vs displacement on a X-Y plotter. Stress and Strain were then calculated from these results using the formulas

$$\sigma = \frac{3 * L * P}{2 * b * h^2} \quad (6)$$

$$\epsilon = \frac{6 * h * \delta}{L^2} \quad (7)$$

where P = load, L = span between rollers on bend fixture, b = sample width, and h = sample height. These equations were utilized to prepare plots of stress verses strain for each sample. The bending modulus, and strain to failure were then determined from these plots.

## **E. SCANNING ELECTRON MICROSCOPY (SEM)**

After bend testing, each half of the sample was prepared for observation of both the polished surface and fracture surface in the SEM. The fracture surface was prepared by coating the sample with a thin film of gold-palladium in a vacuum deposition chamber to provide a conductive coating prior to viewing in the SEM. The samples were then mounted in the SEM, and micrographs were taken of representative sections of the fracture surface.

For microstructure evaluation, the samples were first mounted in cold-mount sample holders, and then polished in a multi-step process that included five grades of grinding paper, an automatic orbital polisher using diamond polishing compound, and a final polish with 0.05  $\mu\text{m}$  alumina. After polishing the samples were again vapor deposited with a film of gold-palladium and backscattered electron micrographs were taken in the SEM.

## **F. GRAIN SIZE DISTRIBUTION**

The grain size distribution of the samples was obtained from the micrographs of the polished surfaces. A tracing of each micrograph was made to provide enough contrast for a high resolution camera to digitize the microstructure. Image processing software from MicroScience (Image Measure Version 4.02, Federal Way, WA), was then utilized to determine the average diameter of the grains by measuring the perimeters of the individual grains. A minimum of eight micrographs of each sample were digitized in this way to provide a statistical average representative of the microstructure.

## G. TRANSMISSION ELECTRON MICROSCOPY

Thin samples were prepared for the TEM by preparing a 3 mm disk of the sample. This disk was thinned by hand to approximately 150  $\mu\text{m}$ , then dimpled to approximately 25  $\mu\text{m}$  in a Gatan, Warrendale, PA, Model 656 precision dimple grinder. Further reduction in thickness was carried out at liquid nitrogen temperatures in a Gatan, Model 600, dual ion milling machine. The samples were studied using both bright field and dark field microscopy. Selected area diffraction patterns (SADP) were also recorded for indexing and identification of the phases observed in the samples. In addition energy dispersive X-ray analysis (EDX) was performed using Kevex software.

### III. RESULTS AND DISCUSSION

#### A. PROPERTIES OF AS-RECEIVED SAMPLES

Table 3 summarizes the properties of the as-received samples. From the chemical composition analysis of the samples it is seen that the amount of  $Y_2O_3$  added during manufacture was the least in 7C, and greatest in 7T. Correspondingly, the amount of oxygen present (in the form of dissolved oxygen and grain boundary  $Al_2O_3$ ) is expected to be maximum in 7C and least in 7T.

The physical properties of the as-received samples are also listed in Table 3. The grain size of the 7C sample is the largest, followed by 7T, and 7R respectively. This is confirmed in Figures 9 through 11 which show backscattered electron SEM images of the samples. The grain size and microstructure are a result of the initial powder preparation and sintering treatment given to the powder compacts (the sintering treatments and forming techniques used are proprietary and not divulged by the manufacturers). The light areas of the microstructure correspond to the yttrium aluminate phases formed by the addition of  $Y_2O_3$  to improve densification through liquid phase sintering. It is also clear from the micrographs that all three samples still have a considerable amount of residual porosity. This is reflected in the density measurements reported in Table 3. The (percent relative density theoretical density) data suggest that the volume fraction of porosity is largest in 7T, and least in 7R.



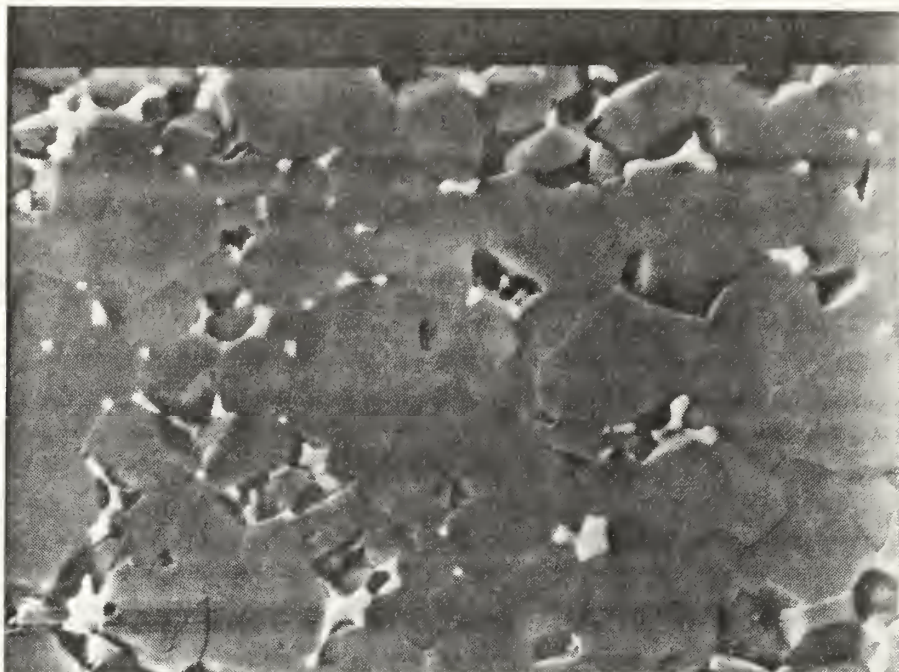


**Figure 9:** As-Received AlN 7C showing the Yttrium-Aluminate phases as small particles at the triple grain junction points.

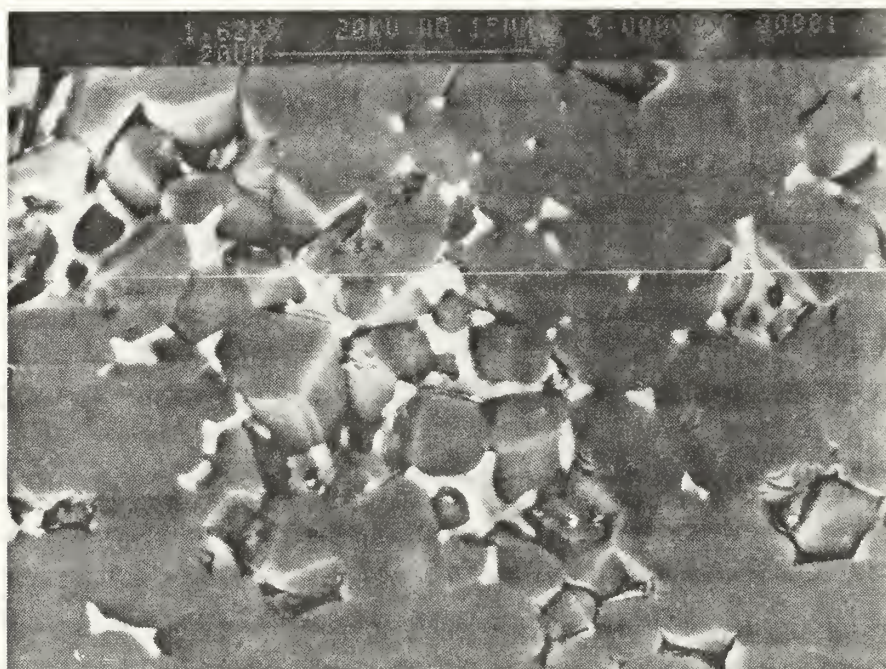


**Figure 10:** As-Received AlN 7T showing evidence of LPS with some residual porosity present.

The micrographs also demonstrate a difference in the morphology and distribution of the yttrium aluminate phases in the samples. The 7C sample shows that the yttrium

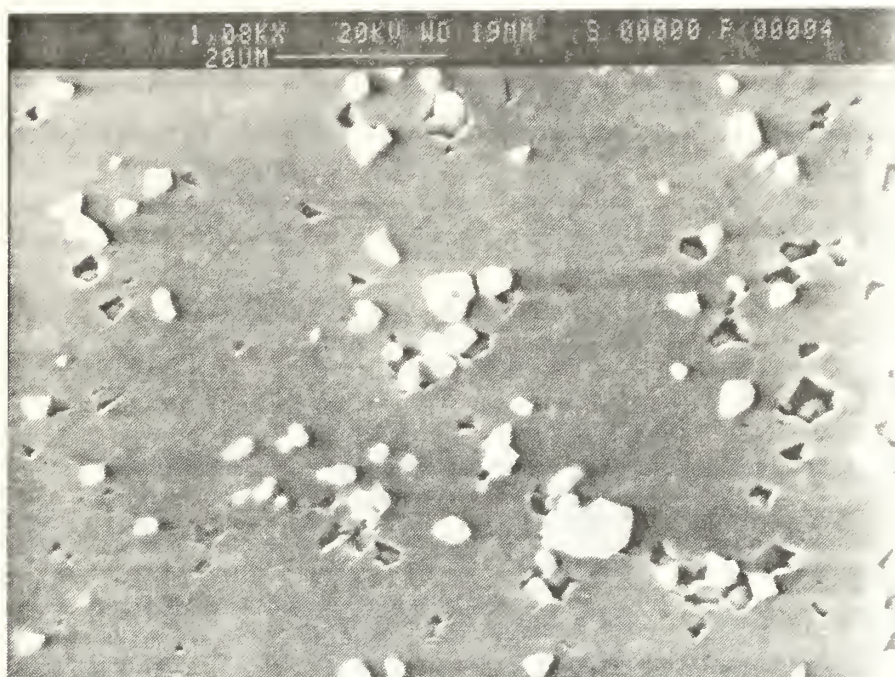


**Figure 11:** As-Received AlN 7R showing the Yttrium-Aluminate phases as chunks of particles approximately the same size as the AlN grains.

aluminate phases are present as relatively small particles at the triple grain junctions, or as thin strips at the grain boundaries. 7T shows similar morphology, with the yttrium aluminate phases present as small particles at triple points, as well as larger chunks between adjacent AlN grains. The 7R sample, however, shows relatively clean grain boundaries with large particles of the yttrium aluminate phases present (4-5  $\mu\text{m}$ ), which are about the same size as the surrounding AlN grains.



**Table 3**  
**Chemical and Physical Properties of As-Received Sintered AlN**

Material/Property	7C	7R	7T
<b><u>Chemical Composition</u></b>			
% Al <sub>2</sub> O <sub>3</sub> in unsintered powder (wt.)	2.41	2.17	1.8
% Y <sub>2</sub> O <sub>3</sub> added to powder (wt.)	1.77	3.79	4.228
% O in sintered product	1.5	1.83	1.7
% Y in sintered product	1.43	2.99	3.33
Second phases present	Al <sub>5</sub> Y <sub>3</sub> O <sub>12</sub> Al <sub>2</sub> Y <sub>4</sub> O <sub>9</sub>	AlYO <sub>3</sub> Al <sub>5</sub> Y <sub>3</sub> O <sub>12</sub>	AlYO <sub>3</sub> Al <sub>5</sub> Y <sub>3</sub> O <sub>12</sub> Al <sub>2</sub> Y <sub>4</sub> O <sub>9</sub>
<b><u>Physical Properties</u></b>			
Grain Size	7.19 ± 3.11 μm	3.26 ± 1.62 μm	6.22 ± 2.54 μm
Theoretical density	3.32 g/cm <sup>3</sup>	3.325 g/cm <sup>3</sup>	3.28 g/cm <sup>3</sup>
Measured density	3.29 g/cm <sup>3</sup>	3.31 g/cm <sup>3</sup>	3.29 g/cm <sup>3</sup>
Relative Density	99.1 %	99.5 %	100 %

## B. PHASE CONSTITUTION OF AS-RECEIVED AND HEAT TREATED AlN

Comparison of the X-ray diffraction patterns of the as-received and heat treated samples reveals the presence of four different yttrium aluminate phases, as well as small amounts of  $\alpha$ -Al<sub>2</sub>O<sub>3</sub>. The yttrium aluminate phases have been coded with respect to the ratio of yttria to alumina for aid in identification on the X-ray diffraction plots. These codes, as well as AlN and  $\alpha$ -Al<sub>2</sub>O<sub>3</sub> with their JCPDS file numbers are included as Table 4.

Table 4  
Identification of Phases Found

Code	Formula	JCPDS Number	Density g/cm <sup>3</sup>
AlN	AlN	25-1133	3.261
Al <sub>2</sub> O <sub>3</sub>	Al <sub>2</sub> O <sub>3</sub>	10-173	3.987
1:1	YAlO <sub>3</sub>	38-222	----
1:1	AlYO <sub>3</sub>	33-41	5.351
3:5	Al <sub>5</sub> Y <sub>3</sub> O <sub>12</sub>	33-40	4.552
2:1	Al <sub>2</sub> Y <sub>4</sub> O <sub>9</sub>	34-368	4.518

The X-ray pattern of the as-received sample of 7C is in the foreground of Figure 12. The large peaks are easily identified as AlN, the primary phase present. Indexing of the remaining peaks reveals the presence of Al<sub>5</sub>Y<sub>3</sub>O<sub>12</sub> and Al<sub>2</sub>O<sub>3</sub>. The presence of  $\alpha$ -Al<sub>2</sub>O<sub>3</sub> was detected only through its most dominant peak at a 2 $\theta$  value of 43.3° (d=

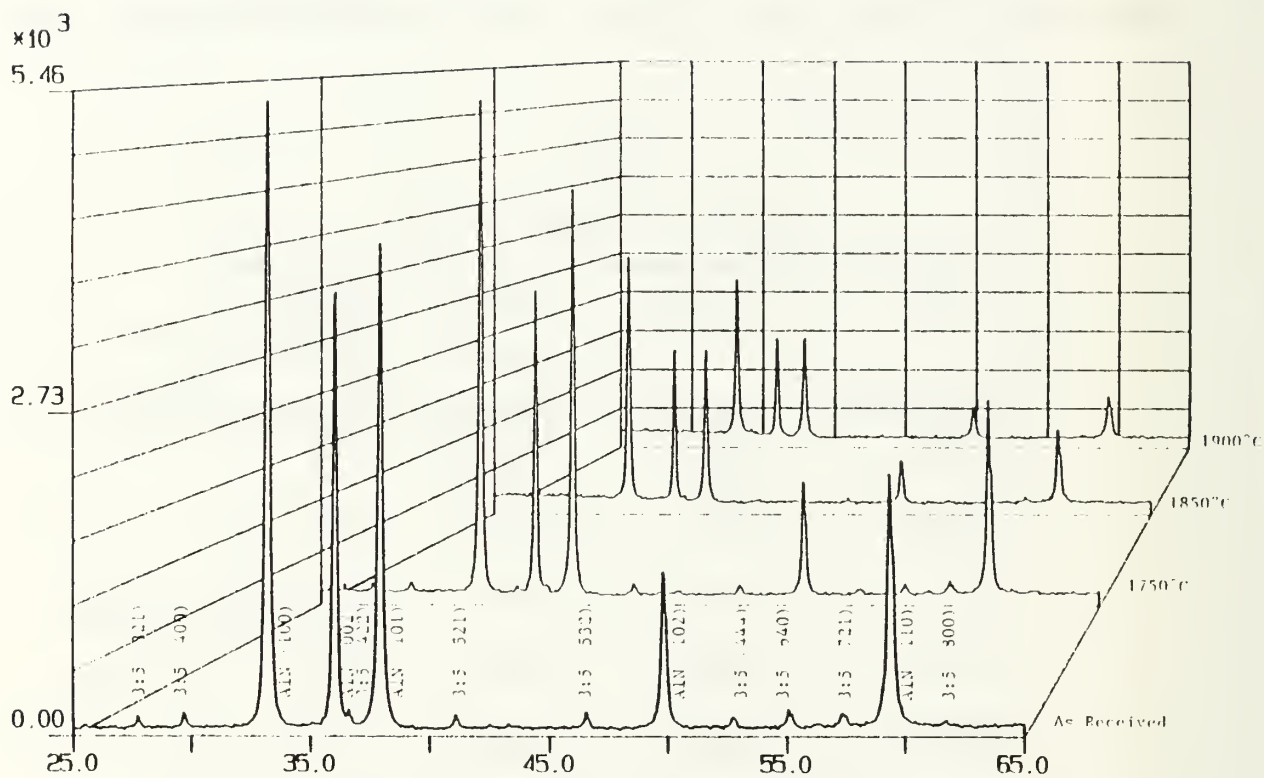


**Figure 12:** X-Ray Diffraction results of AlN 7C, showing decrease in yttrium-aluminate phases with increasing heat treatment.



2.058Å). Later TEM studies also revealed the presence of the  $\text{Al}_2\text{Y}_4\text{O}_9$  phase in the as-received sample.

X-ray diffraction of the 7C sample heat treated at 1750°C revealed the presence of the  $\text{YAlO}_3$  phase although none was found in the as-received state. This cubic phase has been found in samples heated to 1060°C and quenched [Ref.23]. Following the heat treatment at 1750°C, the cooling rate was rapid enough to retain this metastable phase which formed at high temperatures.  $\text{YAlO}_3$  does not occur on the phase diagram for the  $\text{Y}_2\text{O}_3$ - $\text{Al}_2\text{O}_3$  system which is shown in Figure 13 [Ref.24]. Two possible reasons for the formation of  $\text{YAlO}_3$  are:

a)  $\text{Al}_2\text{Y}_4\text{O}_9$  and  $\text{Al}_5\text{Y}_3\text{O}_{12}$  may combine at elevated temperatures to form  $\text{YAlO}_3$ , which is stoichiometrically between the two compounds.

b)  $\text{Al}_5\text{Y}_3\text{O}_{12}$  dissociates at high temperatures to give a two-phase mixture of  $\text{YAlO}_3$  and  $\alpha\text{-Al}_2\text{O}_3$ . However, at the present time, it is not clear which of these two mechanisms is operating.

Some reduction in the amount of  $\text{Al}_5\text{Y}_3\text{O}_{12}$  relative to the as-received state is also observed.

Around 1850°C a liquid is formed in the  $\text{Y}_2\text{O}_3$ - $\text{Al}_2\text{O}_3$  system in the 19-42 wt. % composition range. After the 1850°C heat treatment a decrease in the relative intensities of both  $\text{YAlO}_3$  and  $\text{Al}_5\text{Y}_3\text{O}_{12}$  peaks are seen. This can be attributed to either liquification followed by evaporation, or to sublimation of the yttrium aluminate phases. Although evaporation/sublimation at 1850°C is not predicted by the phase diagram (Figure 13), the nitrogen atmosphere employed during heat treatment may influence this behavior. This

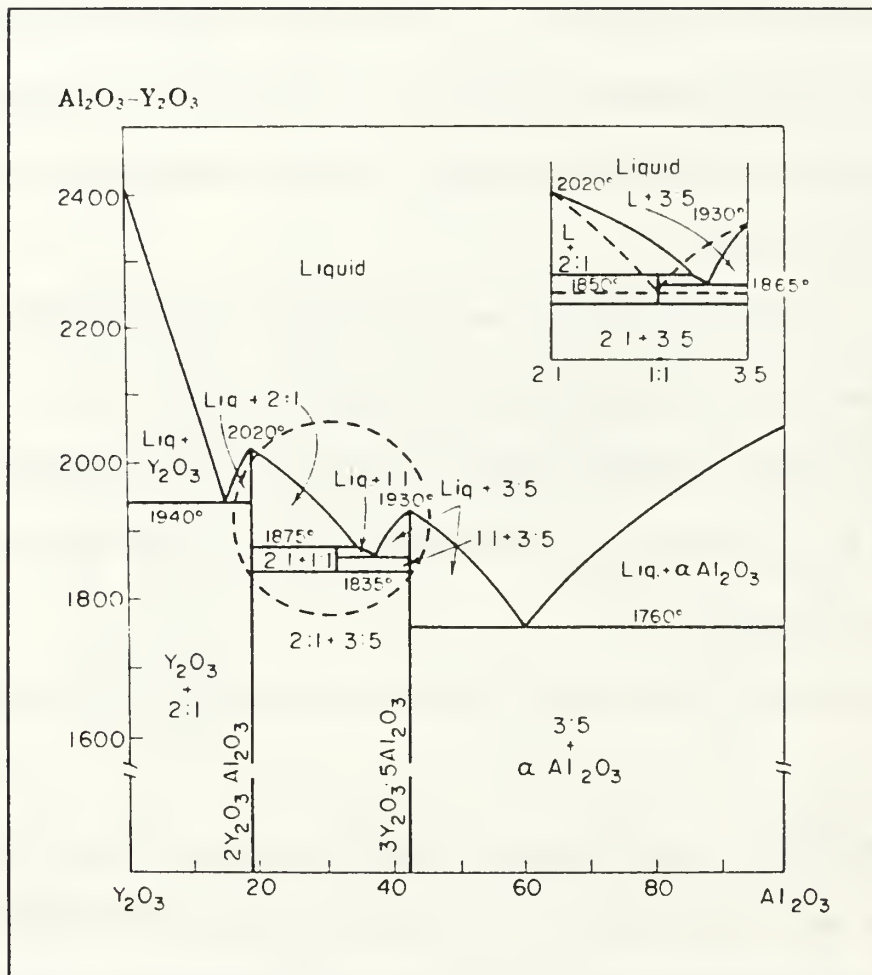


Figure 13: Phase Diagram of  $\text{Al}_2\text{O}_3\text{-Y}_2\text{O}_3$  system [Ref.24].

possibility is supported by the presence of a yellowish deposit on the sample holders after heat treatment. The color of  $Y_2O_3$  is listed in reference 25 as yellowish, suggesting that a yttrium bearing oxide redeposited on the surrounding areas during cooling [Ref.25].

After an extended heat treatment at  $1850^{\circ}C$  for 7 hours, the amounts of detected yttrium aluminate phases are reduced even further. After heat treatment at  $1900^{\circ}C$  no yttrium aluminate phase is detected in XRD, suggesting increasing dissociation/evaporation/sublimation with progressively high temperatures and times above  $1850^{\circ}C$ .

The X-ray patterns for the as-received 7T sample contain three yttrium aluminate phases.  $AlYO_3$  is a 1:1 yttria-alumina phase with an orthorhombic structure that appears as a metastable phase around  $1835^{\circ}C$  [Figure 14]. This compound has been found to form at a lower temperature ( $1675^{\circ}C$ ) over extended periods of time [Ref.26]. In addition to the  $Al_2Y_4O_9$  phase and  $\alpha-Al_2O_3$ , as-received 7T contains more  $Al_5Y_3O_{12}$  phase than the as-received 7C. This can be explained by the increased amount of yttria added as a sintering aid (four percent vs. one-point-eight percent, Table 3).

Heat treatment of the 7T samples produced an initial decrease in the yttrium aluminate phases present. The  $AlYO_3$  phase, which is present metastably, initially decreases, possibly due to decomposition into  $Al_5Y_3O_{12}$  and  $Al_2Y_4O_9$  phases. This should lead to an increase in the  $Al_5Y_3O_{12}$  phase, although this is not observed in the XRD results possibly due to sublimation/evaporation. Upon heat treating at  $1850^{\circ}C$  for two hours, there is a significant decrease in the amount of  $AlYO_3$  present as more is converted to  $Al_5Y_3O_{12}$  and  $Al_2Y_4O_9$ . Further heating at this temperature produces a

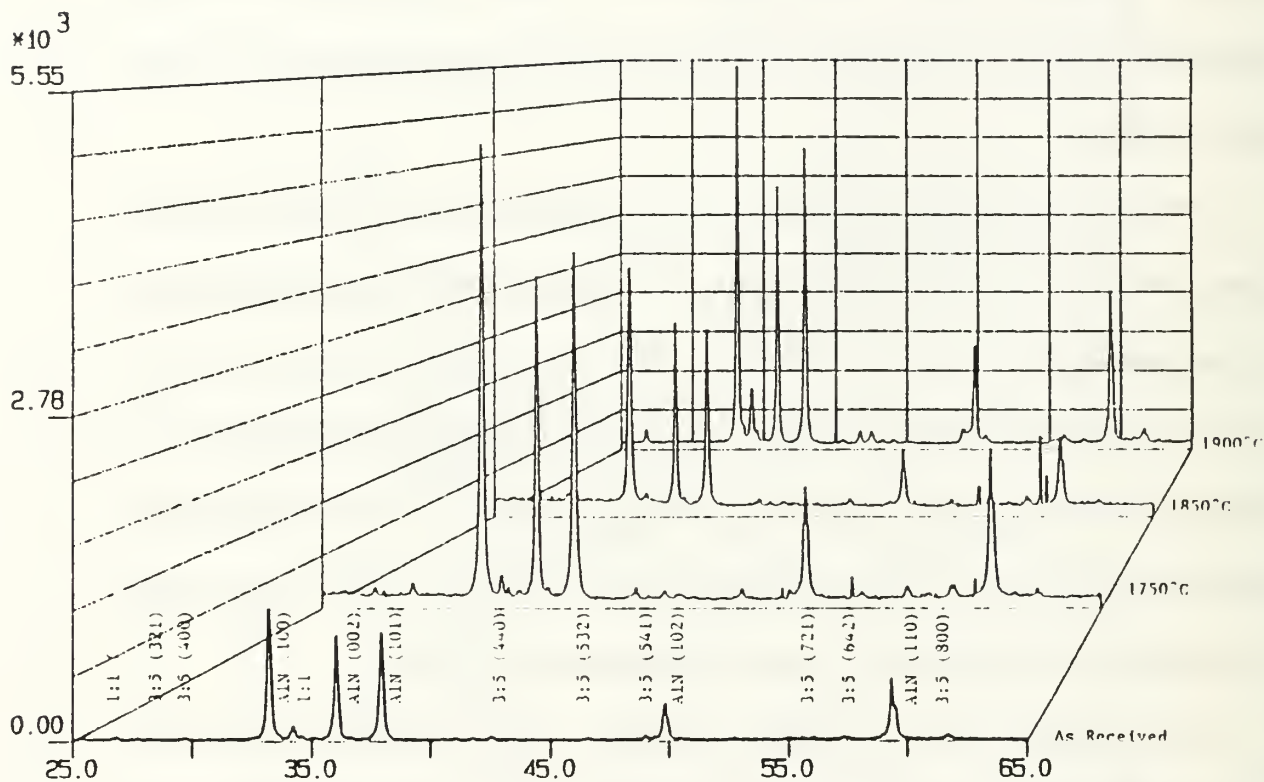


**Figure 14:** X-Ray Diffraction results of AlN 7T showing increase of  $\text{Al}_2\text{O}_3$  at higher heat treatment.

reversal in the trend for the reduction of  $\text{AlYO}_3$ . Since  $\text{AlYO}_3$  is stable above  $\approx 1850^\circ\text{C}$ , it forms again from the available  $\text{Al}_5\text{Y}_3\text{O}_{12}$  and  $\text{Al}_2\text{Y}_4\text{O}_9$ , producing a further reduction in  $\text{Al}_5\text{Y}_3\text{O}_{12}$ . Upon heating to  $1900^\circ\text{C}$  a marked increase in the amount of  $\text{AlYO}_3$  is seen, indeed more than that present than in the as-received sample. As in 7C, confirmed reduction in the amount of  $\text{Al}_5\text{Y}_3\text{O}_{12}$  is also observed at progressively higher temperatures due to evaporation. Additional reduction of  $\text{Al}_5\text{Y}_3\text{O}_{12}$  occurs due to formation of  $\text{Al}_2\text{Y}_4\text{O}_9$  in 7T.

The X-ray data in Figure 15, for the 7R samples follows a trend similar to the 7T samples, as expected from the amount of yttria added. As less yttria was added to this sample than the 7T sample, less  $\text{AlYO}_3$  is present in the as-received material.  $\text{AlYO}_3$  and  $\text{Al}_5\text{Y}_3\text{O}_{12}$  decrease at  $1750^\circ$  and  $1850^\circ\text{C}$  with  $\text{AlYO}_3$  increasing at  $1900^\circ\text{C}$  and  $\text{Al}_5\text{Y}_3\text{O}_{12}$  disappearing completely. This is again explained by the evaporation of  $\text{Al}_5\text{Y}_3\text{O}_{12}$  conversion to  $\text{AlYO}_3$ .

## **C. CHANGES IN MICROSTRUCTURE AND PROPERTIES WITH HEAT TREATMENT**

### **1. Scanning Electron Microscope (SEM) Study**

The microstructure of the samples showed significant change after heat treatment. Initially the 7C sample showed appreciable porosity with the yttrium aluminate phases present as small particles occupying positions at the triple points, and along the grain boundaries as thin strips. This indicates that the temperatures during sintering were high enough to produce liquid-phase sintering (LPS). After heat treatment



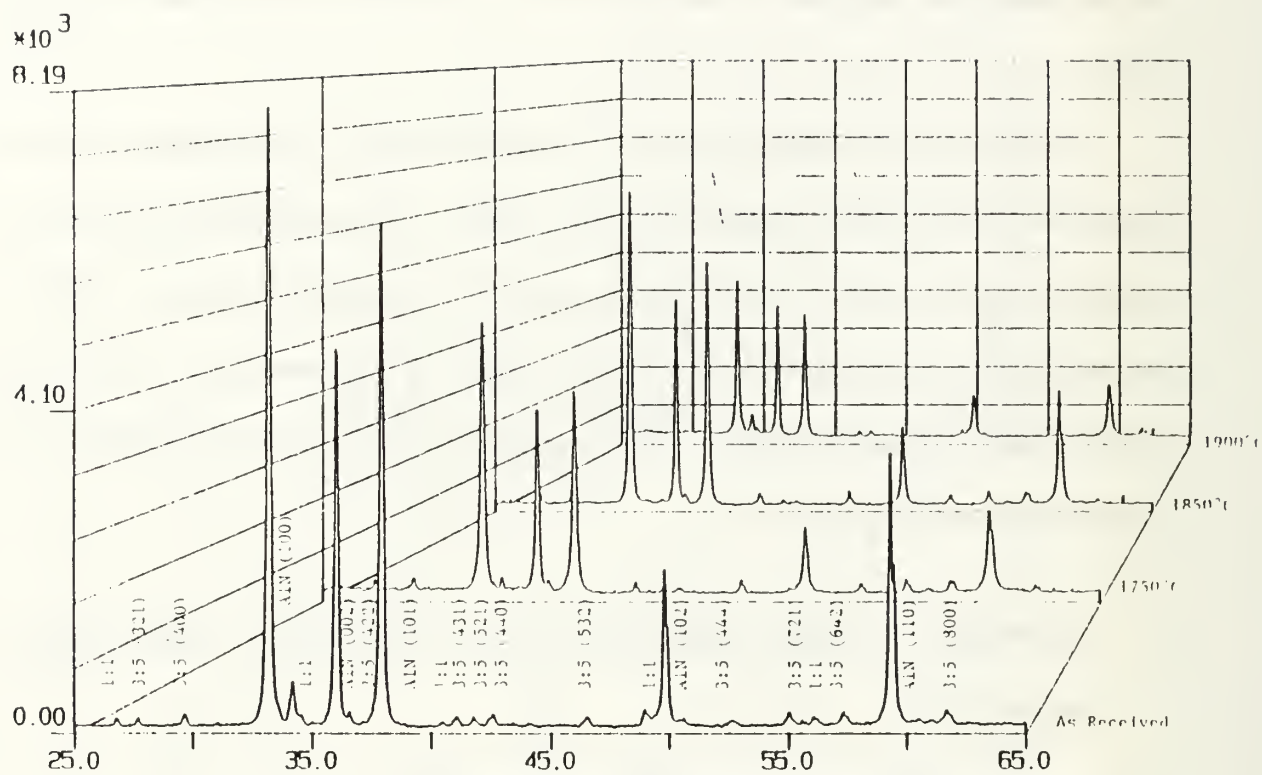
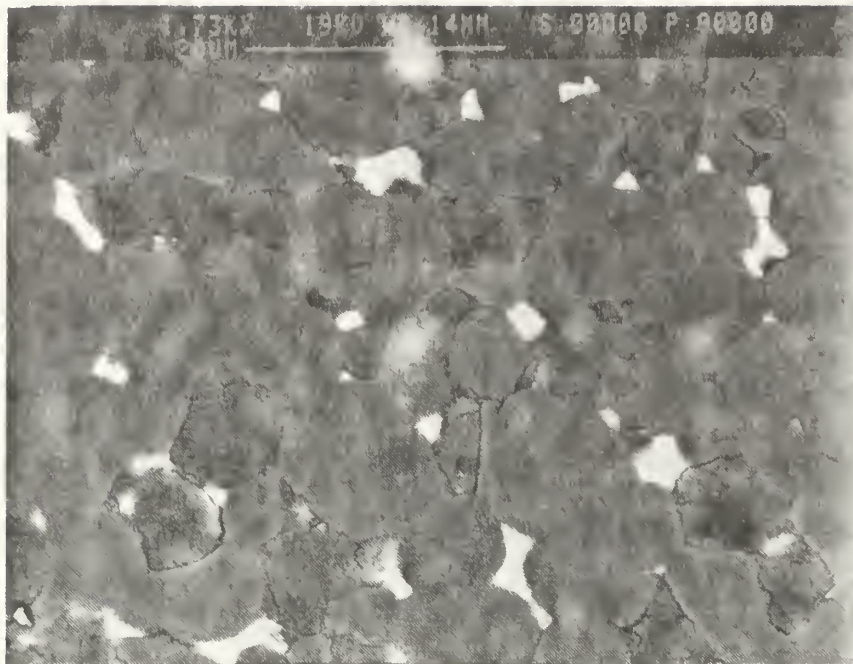


Figure 15: X-Ray Diffraction results of AlN 7R, showing increase of  $\text{Al}_2\text{O}_3$  with increasing heat treatment.

at 1750°C for two hours (Figure 16), much of the porosity has been eliminated, which corresponds to the initial increase in density reported in Table 5. The yttrium aluminate phases now appear predominantly as small particles at the triple grain points, suggesting appreciable LPS.

After heat treatment at 1850°C for two hours, there is further evidence of LPS taking place (Figure 17). The grains have become more rounded, and the phases at the triple points more triangular. LPS can occur at temperatures as low as 1760°C in the presence of only  $\text{Al}_5\text{Y}_3\text{O}_{12}$  and  $\text{Al}_2\text{O}_3$  as evident from Figure 13. Little data is available about the  $\text{YAlO}_3$  phase that is produced at 1750°C. In the presence of  $\text{Al}_5\text{Y}_3\text{O}_{12}$  and  $\text{Al}_2\text{Y}_4\text{O}_9$ , however, the minimum temperature for LPS to occur is  $\approx 1865^\circ\text{C}$ - $1875^\circ\text{C}$  according to the available phase diagram. It is possible that the presence of  $\text{YAlO}_3$ , together with the other phases, can form a liquid phase at temperatures as low as  $\approx 1750^\circ\text{C}$ , resulting in the observed liquid phase sintering. However, this possibility needs to be investigated further. After treatment at 1900°C (Figure 18), the rounding of the  $\text{AlN}$  grains is even more pronounced.

The as-received sample of 7T also shows evidence of LPS (Figure 10), with the yttrium aluminate phases present primarily at the triple points. Despite LPS, there was appreciable residual porosity in this sample. This porosity appeared to be reduced significantly during heat treatment, especially after heat treatment at 1900°C (Figure 19). Comparison of the samples of 7C and 7T after heat treatment at 1900°C reveals a larger amount of yttrium aluminate phases in the 7T samples. This is expected since a larger amount of yttrium oxide was added to 7T (Table 3). Also of note is the more



**Figure 16:** AlN 7C After heat treatment at 1750°C for 2-hours, showing densification, reduction of pores, and relocation of yttrium-aluminate to triple points.

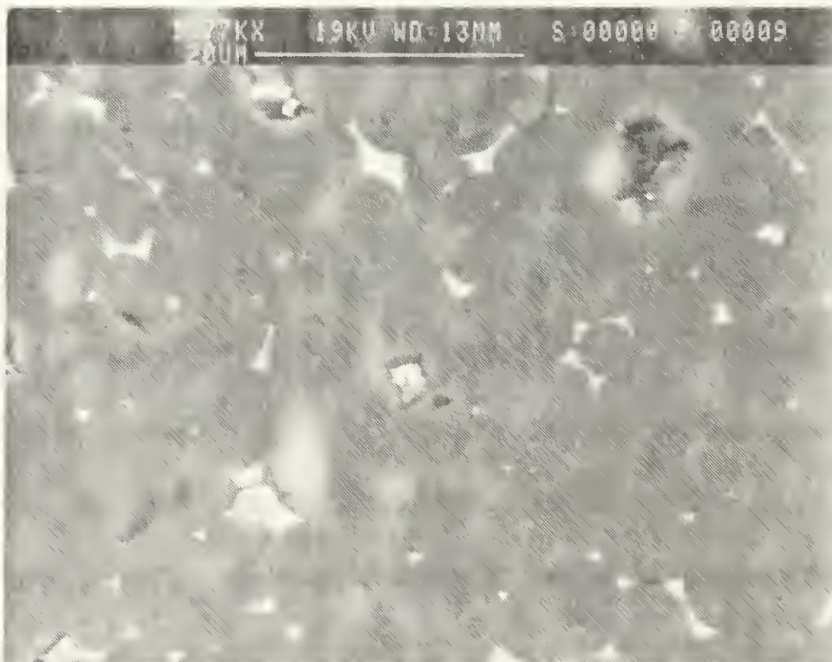


**Figure 17:** AlN 7C after heat treatment at 1850°C for 2 hours, showing further evidence of LPS.



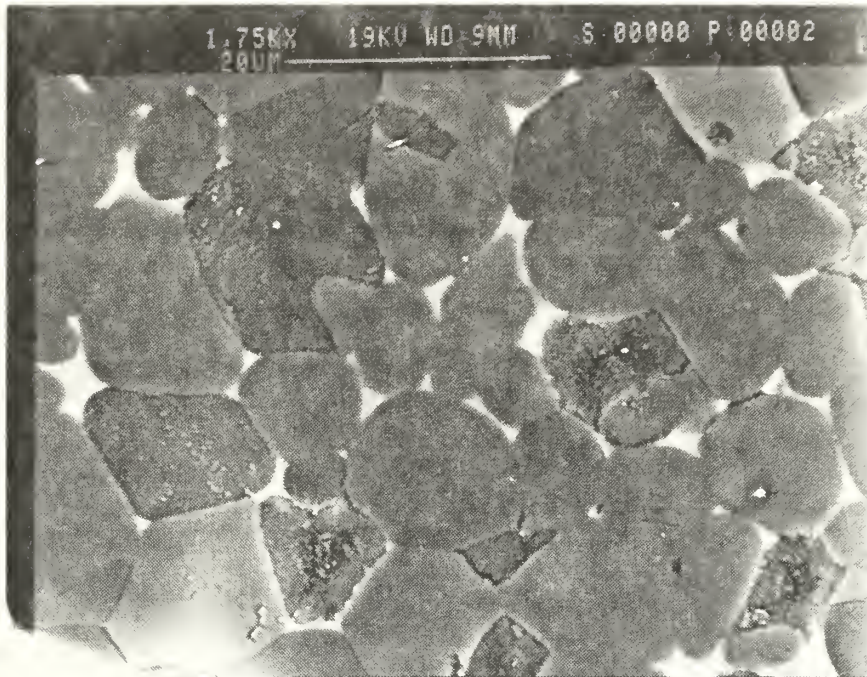


**Figure 18:** AlN 7C after heat treatment at 1900°C for 2 hours, showing further evidence of LPS.

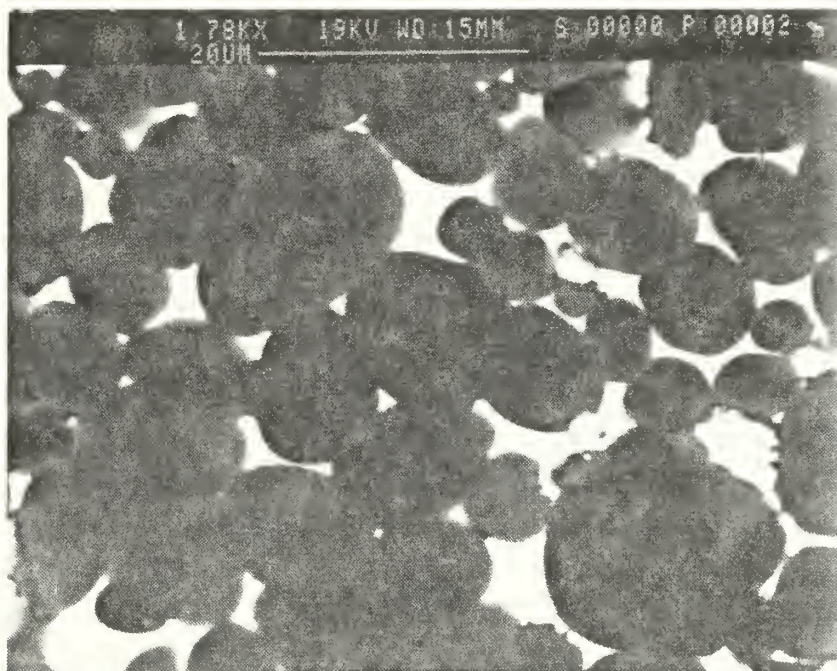


**Figure 19:** AlN 7T after heat treatment at 1900°C for 2 hours, showing significant evidence of LPS, rounded grains, and greater presence of yttrium-aluminate phases compared to 7C.

pronounced rounding of the 7T grains versus 7C due to extensive LPS, as expected for the greater amount of aluminate phases in 7T.

The initial microstructure of the 7R sample shows a much finer grain size distribution, and little evidence of LPS (chunks of yttrium aluminates are visible). Heat treatment at 1750°C does not appear to have resulted in liquefaction of the yttrium aluminate phases (as evidenced from Figure 20). Heat treatment at 1900°C, however, did result in redistribution of the yttrium-aluminate phases to the triple grain junctions and along grain boundaries indicating LPS (Figure 21). Thus it is apparent that LPS in this system begins between 1750°C and 1900°C.

## **2. Grain Size Distribution**

The results of the grain size analysis of the SEM micrographs are presented in Figure 22, and Table 5. They clearly reveal that the 7C samples have the largest grains, followed by the 7T and 7R. Heat treatment of the samples at 1750°C produces a slight increase in grain size in all three samples. As the phase diagram shows, there are no liquids present at this temperature (Figure 13). In the absence of the liquid phase, the primary method of grain growth would be through the motion of individual atoms of the small grains to the large grains to reduce the free energy [Ref.15]. After heat treatment at 1850°C there is a slight increase in the grain size. At this temperature there is evidence of LPS taking place. Since a solid skeleton is already present, a minimal degree of rearrangement of the AlN grains by sliding is present, constituting the first stage of LPS. Primarily the second stage, or accommodation stage, where smaller particles, and regions of high free energy, are dissolved into solution, and recrystallize



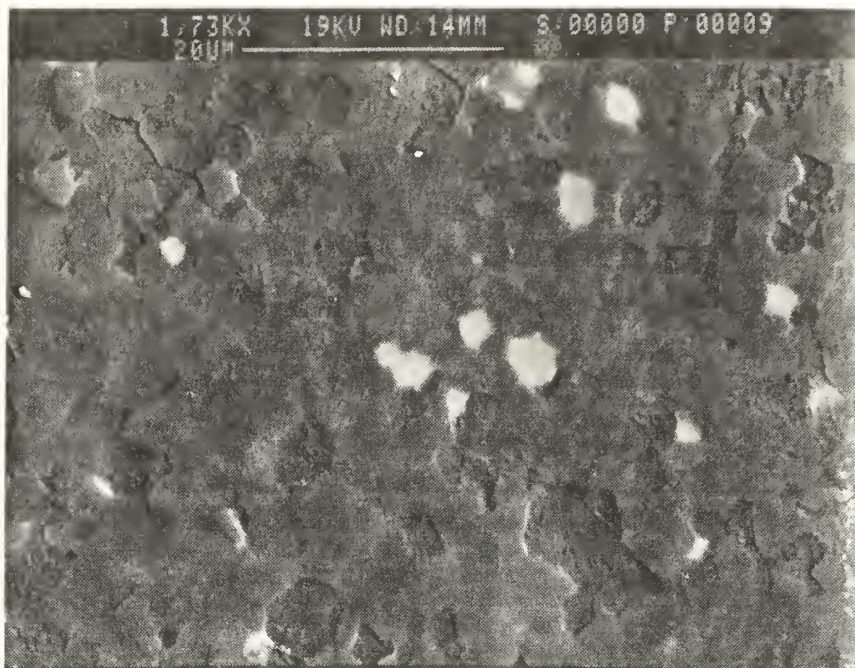


**Figure 20:** AlN 7R after heat treatment at 1750°C for 2 hours, showing no evidence of LPS.

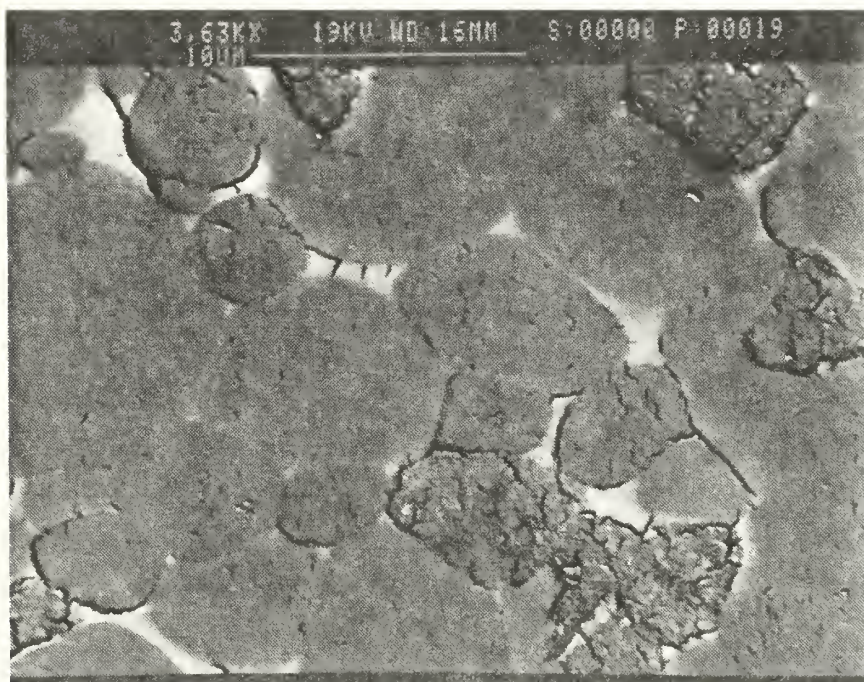


**Figure 21:** AlN 7R after heat treatment at 1900°C for 2 hours, showing LPS has occurred between 1750° and 1900°C.

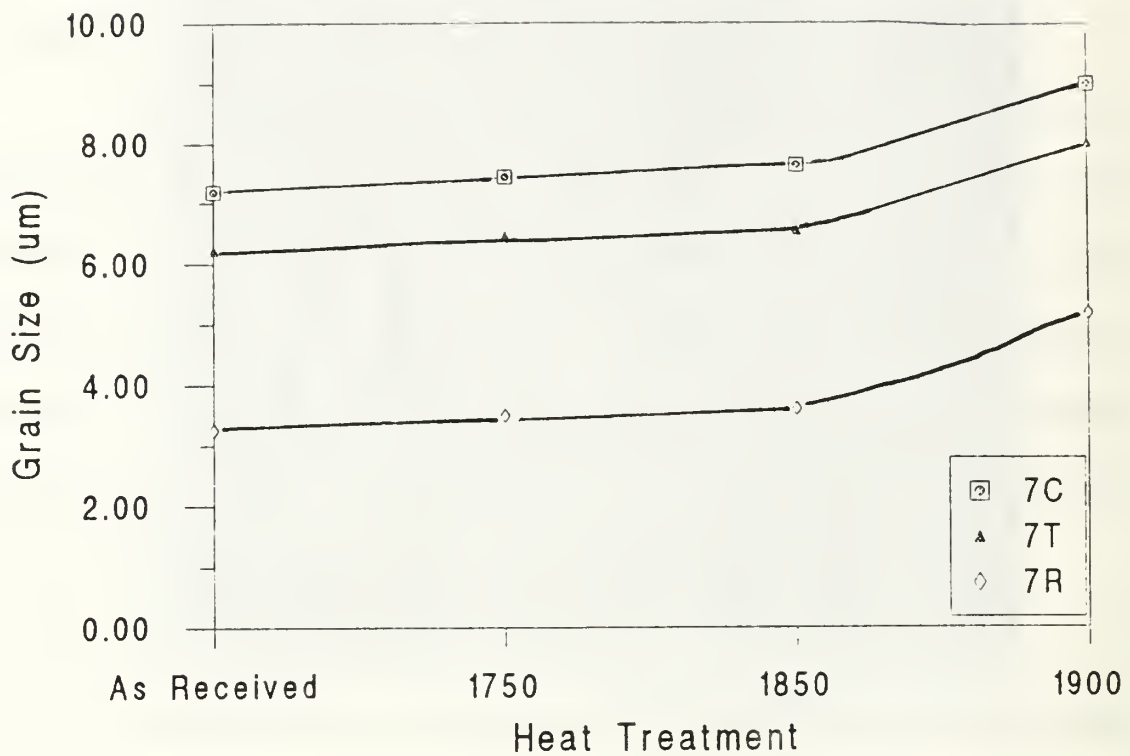


**Figure 22:** Grain Size distribution of AlN Samples showing increasing diameter with heat treatment temperature with a significant increase at 1900°C.

Table 5 Grain Size Distrubution			
Material/Heat Treatment	7C	7T	7R
As Received	7.19 ± 3.11μm	6.22 ± 3.11μm	3.26 ± 1.62μm
1750	7.44 ± 3.34μm	6.45 ± 2.25μm	3.51 ± 1.20μm
1850	7.64 ± 2.85μm	6.54 ± 2.51μm	3.60 ± 1.35μm
1900	9.02 ± 3.76μm	8.04 ± 3.34μm	5.18 ± 2.08μm

in areas of lower energy is expected to be operative [15]. This is seen as rounding of the corners of the grains. This stage of LPS is just starting to take place at this time and temperature, and as such has not resulted in a large increase in grain size. At 1900°C the grains have grown significantly. The presence of greatly rounded grains is direct evidence of the second stage of LPS taking place (Figure 18). The elevated temperature has accelerated the process, resulting in a significant grain size increase which is abetted by solid state sintering, constituting the third stage of LPS.

### 3. Density Changes Due to Sintering

The density measurements reveal differences in the response of the samples to heat treatment, commensurate with the phases produced. This data is recorded in Table 6. The data for 7C is also plotted in Figure 23 as a function of the sintering temperature. The data for 7T and 7R showed large scatter, probably because of a very non-uniform distribution of the yttrium aluminates, resulting in different densities at different locations within the same batch. In the 7C sample, density decreases during the initial heat treatment at 1750°C. An increase in density is usually expected due to the elimination of porosity. However, the production  $YAlO_3$  probably offsets this increase. Continued heat treatment results in a stabilization of the density around 3260 kg/m<sup>3</sup>. This is due to the evaporation of the yttrium aluminate phases and simultaneous densification. This final density is in fair agreement with the density of pure AlN. X-ray analysis of 7C after 1900°C confirms that most of the yttrium aluminate phases are gone at this stage, with only a small amount of  $Al_2O_3$  present.



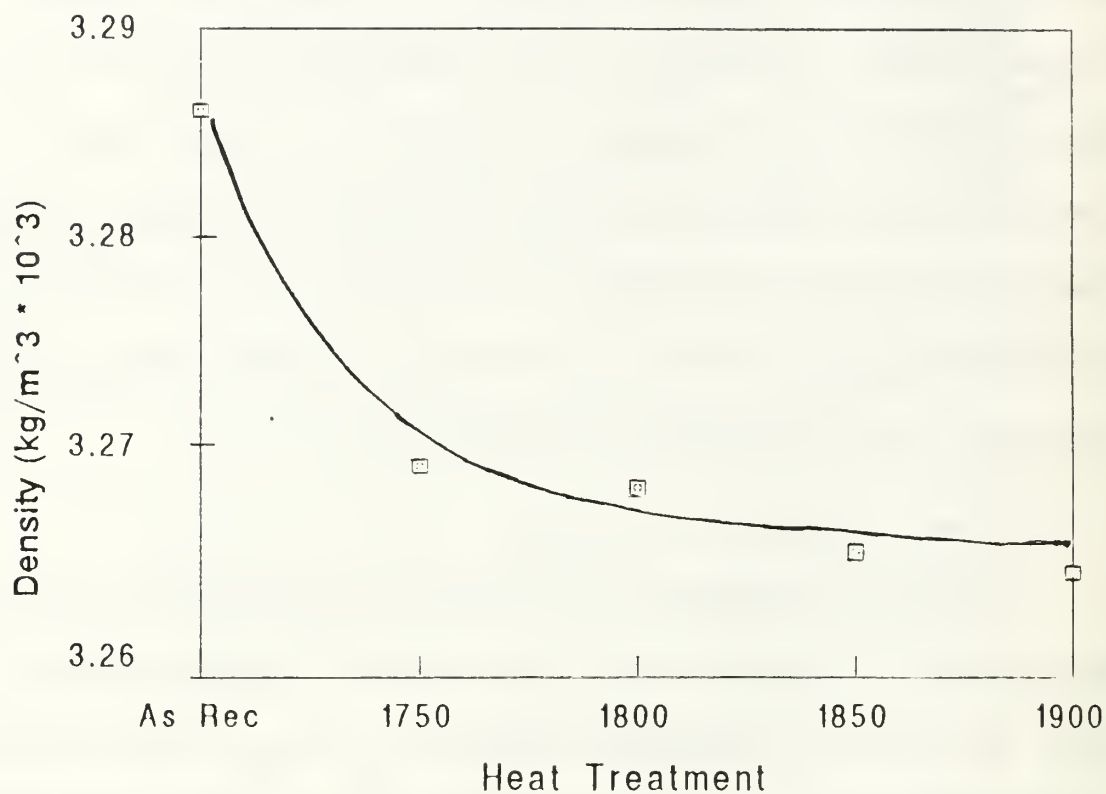


**Figure 23:** AlN 7C Density after heat treatment, showing decrease in density with heat treatment leveling off at higher temperatures.

**Table 6**  
**AlN Density Data**

Heat Treatment	7C	7T	7R
As Received	3.268	3.310	3.289
1800	3.269	3.351	3.311
1800	3.268	3.293	3.352
1850	3.265	3.321	3.360
1900	3.259	3.318	3.332

#### 4. Mechanical Properties

The variation of modulus in bending ( $E_b$ ) and the strain to fracture ( $\epsilon_b$ ) of 7C and 7T with sintering temperature are shown in Figures 24 and 25, and recorded in Tables 7 and 8 respectively. In the 7C samples,  $E_b$  first drops at 1750°C, then rises at 1800°C and 1850°C and drops back at 1900°C. SEM of the fracture surface of the as-received sample (Figure 26), reveals intergranular fracture as the primary mode of failure, although some transgranular regions were also formed. After heat treatment at 1750°C (Figure 27), the failure mode became primarily transgranular, and revealed numerous microfissures that appeared to originate in the grain boundary phase. The observed change in fracture mode is associated with the formation of  $YAlO_3$ . Microcracks that form at the grain boundary phase prefer to travel through the brittle intergranular phase. However, not finding a continuous network of brittle intergranular phases, they propagate in a transgranular manner. Many of the cracks do not lead to eventual failure and leave the microfissures observed in Figures 27 and 28. While these microfissures do not contribute to the final failure they do result in a decrease in the bending modulus, and an increase in the overall strain to fracture.

As the heat treatment temperature is increased, the mode of fracture transitions back to intergranular (Figures 28 and 29). This may be due to the reduction in the grain boundary  $YAlO_3$ . Commensurately the microfissuring decreases and bending modulus increases.

After sintering at 1900°C, the fracture surface shows transgranular failure and can be related to improved sintering (liquid phase and solid state). Even though loss



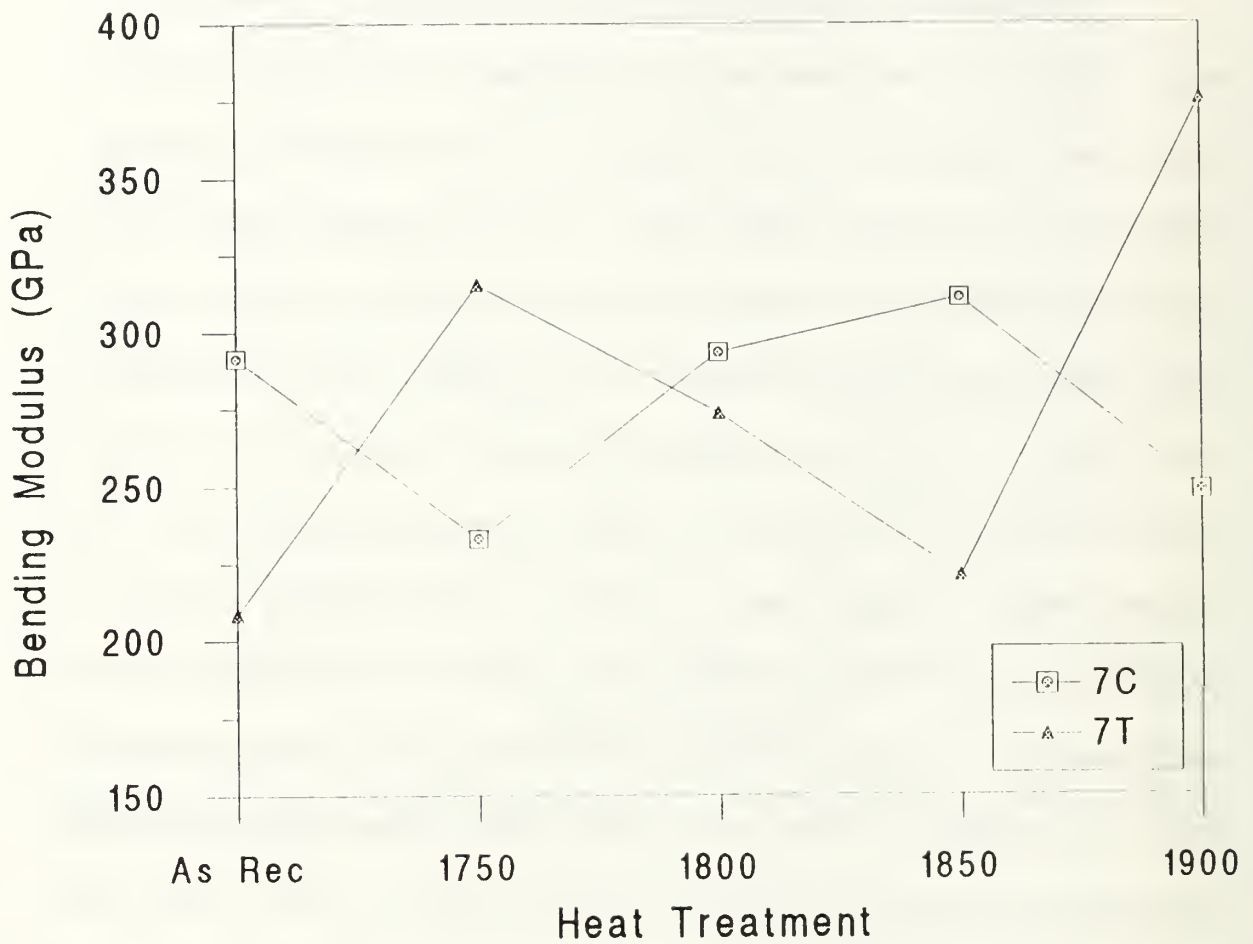


Figure 24: Bending Modulus of 7C and 7T samples as a function of heat treatment.

Table 7 Bending Modulus Data					
Heat Treatment	As Received	1750°C	1800°C	1850°C	1900°C
Bending Modulus	GPa	GPa	GPa	GPa	GPa
7C	291.4	233.1	293.0	310.7	248.5
7T	208.4	315.2	273.4	220.8	375.8

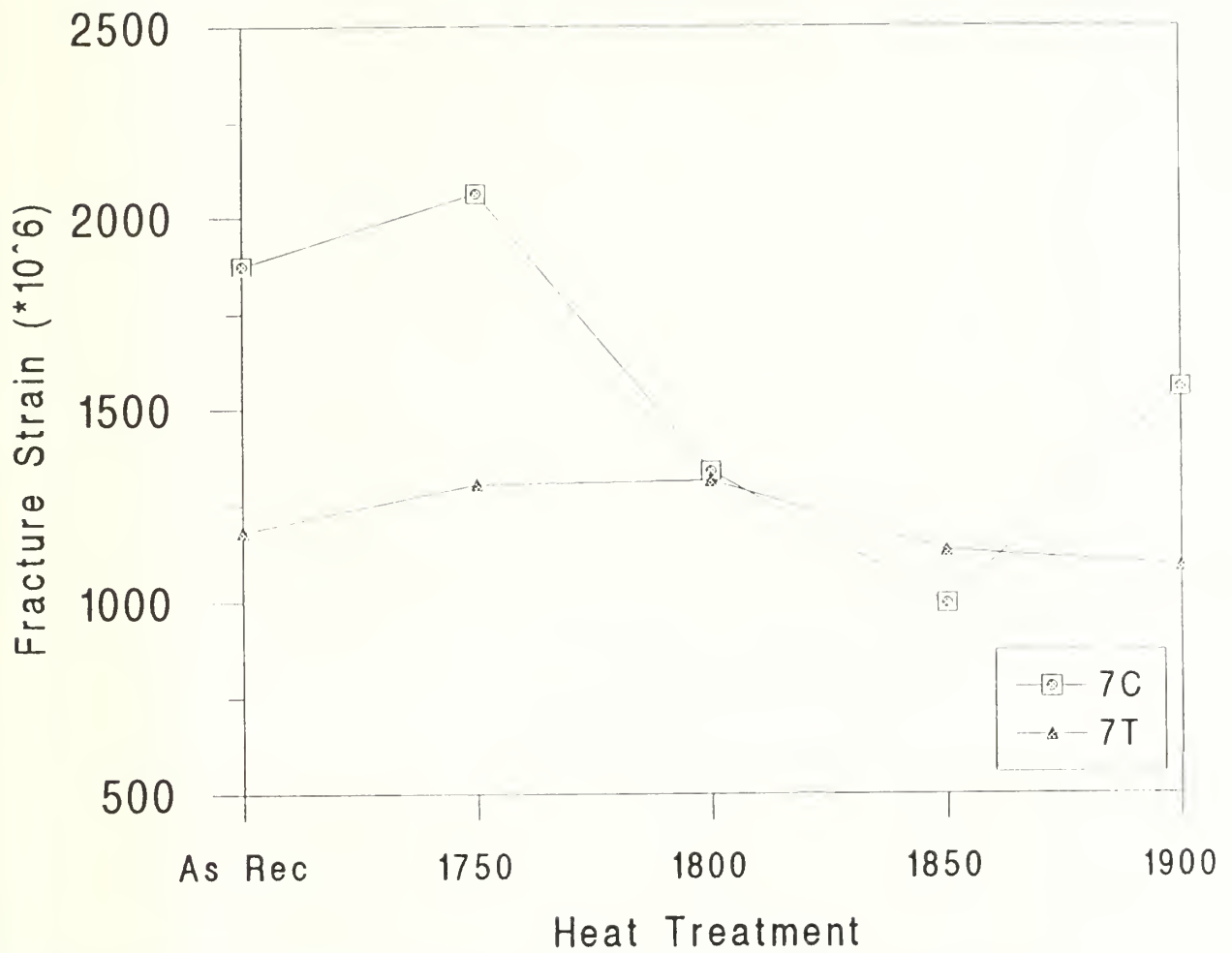
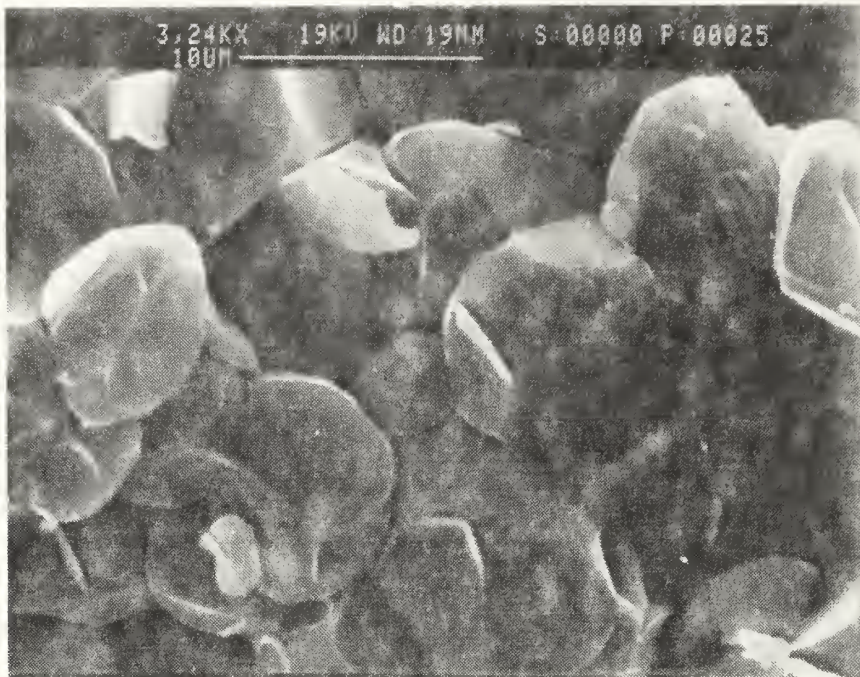
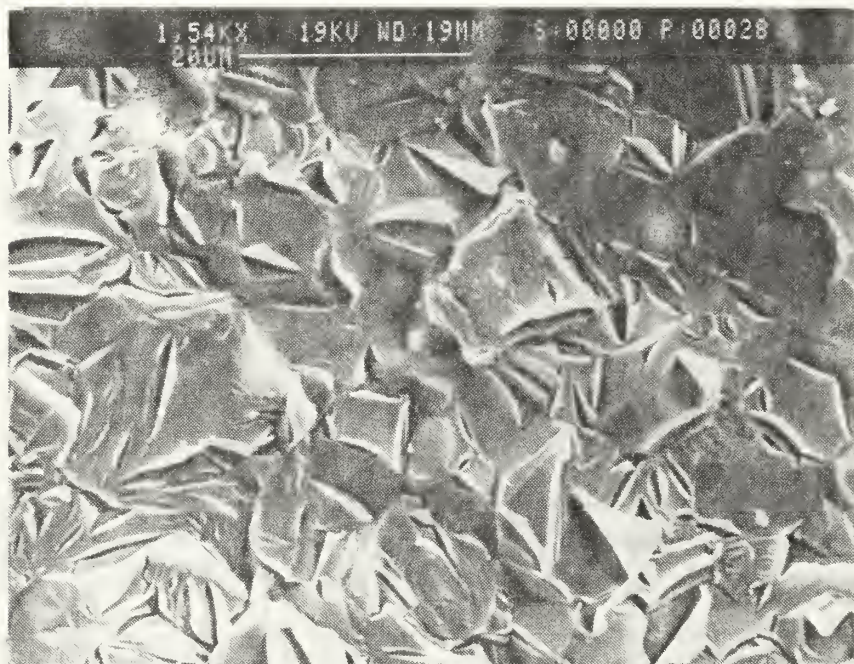


Figure 25: Strain to Failure of 7C and 7T samples as a function of heat treatment.

Table 8 Strain to Failure Data					
Heat Treatment	As Received	1750°C	1800°C	1850°C	1900°C
Strain to Failure	$\times 10^{-6}$	$\times 10^{-6}$	$\times 10^{-6}$	$\times 10^{-6}$	$\times 10^{-6}$
7C	1874.2	2061.7	1337.9	994.8	1555.8
7T	1180.8	1303.0	1212.7	1131.2	1091.7



**Figure 26:** SEM micrograph of fracture surface of 7C sample as received, showing primarily intergranular fracture.



**Figure 27:** SEM micrograph of fracture surface of 7C sample after heat treatment at 1750°C, showing introduction of microfissures and change in mode to transgranular fracture.



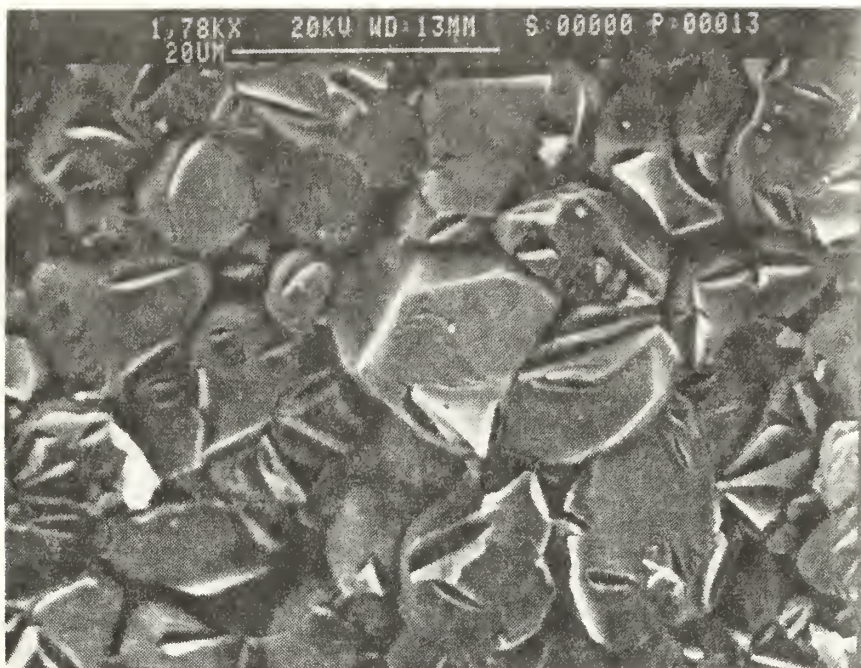


**Figure 28:** SEM micrograph of fracture surface of 7C sample after heat treatment at 1800, showing reduction in microfissures, and transition to intergranular fracture.

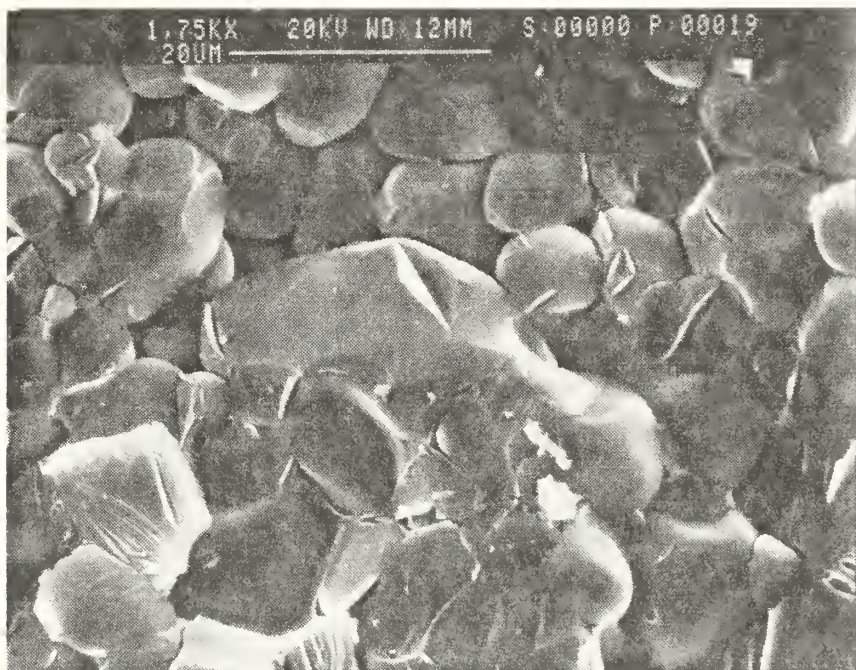


**Figure 29:** SEM micrograph of fracture surface of 7C sample after heat treatment at 1850°C, showing primarily intergranular fracture.

of the aluminate phases occurs (Figure 12), a small but significant amount of the grain boundary aluminate phase is still present and results in the microfissures seen in Figure 30. As before, these features lead to a drop in the bending modulus and an increase in the strain to fracture. At 1800°C and 1850°C loss of the aluminate phases occurs, but the sintering processes are not fast enough to result in compensatory densification, thereby leading to intergranular fracture. At the higher temperature, (1900°C), LPS begins and promotes a more compact material resulting in transgranular failure, although some pockets of poorly sintered material still remain, and result in some intergranular failure. This type of fracture was probably in regions where the yttrium aluminate phases were absent during the heat treatment, and adequate solid state sintering did not occur to give strong AlN grain boundaries.

The as-received 7T sample shows mixed-mode intergranular/transgranular fracture. The transgranular regions showed some microfissures (Figure 31). After heat treatment at 1750°C, 1800°C, and 1850°C, the fracture mode progressively becomes more intergranular (Figures 32 - 34), with a concurrent decrease in  $E_b$ . At 1900°C, however, the mode transitions to transgranular in nature (Figure 35), with a concurrent increase in  $E_b$ . Sintering at 1900°C causes sintering (both liquid phase and solid state), between grains, resulting in significant reduction in porosity, and therefore an increase in  $E_b$ .

It should be noted that in 7T a higher  $E_b$  is associated with transgranular failure and a higher amount of  $AlYO_3$ . On the other hand, in 7C, transgranular failure





Figure 30: SEM micrograph of fracture surface of 7C sample after heat treatment at 1900°C, showing transition back to transgranular fracture and reappearance of microfissures.

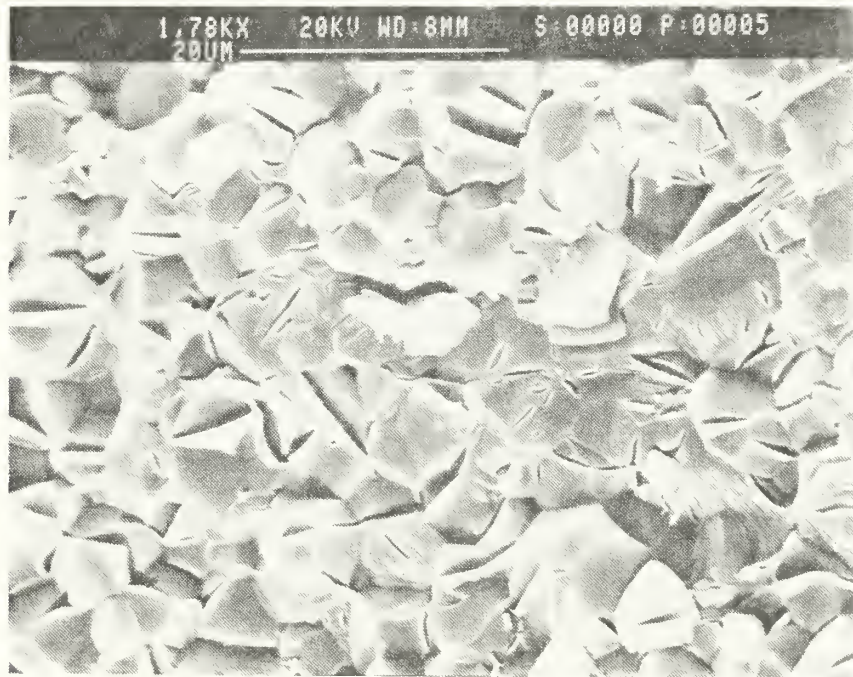
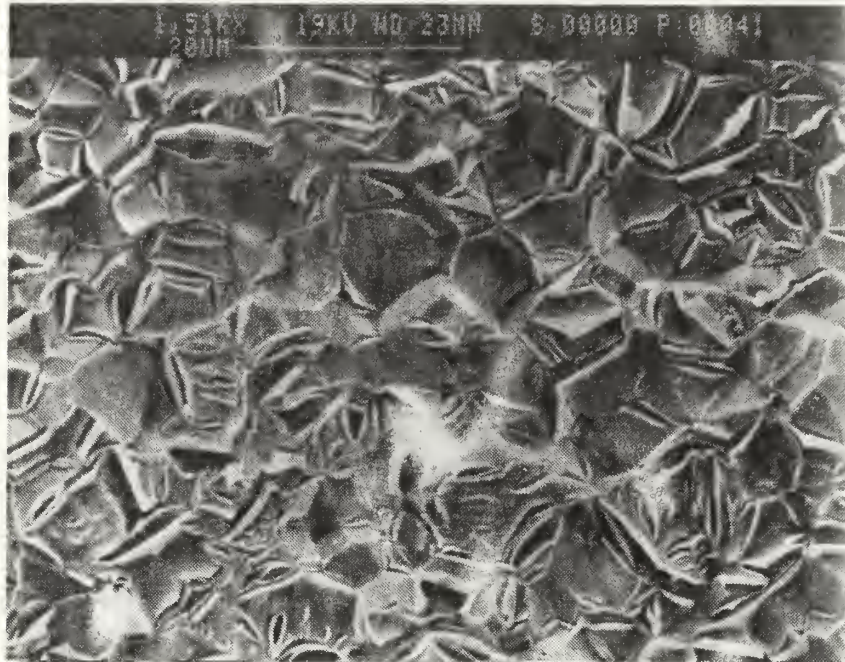
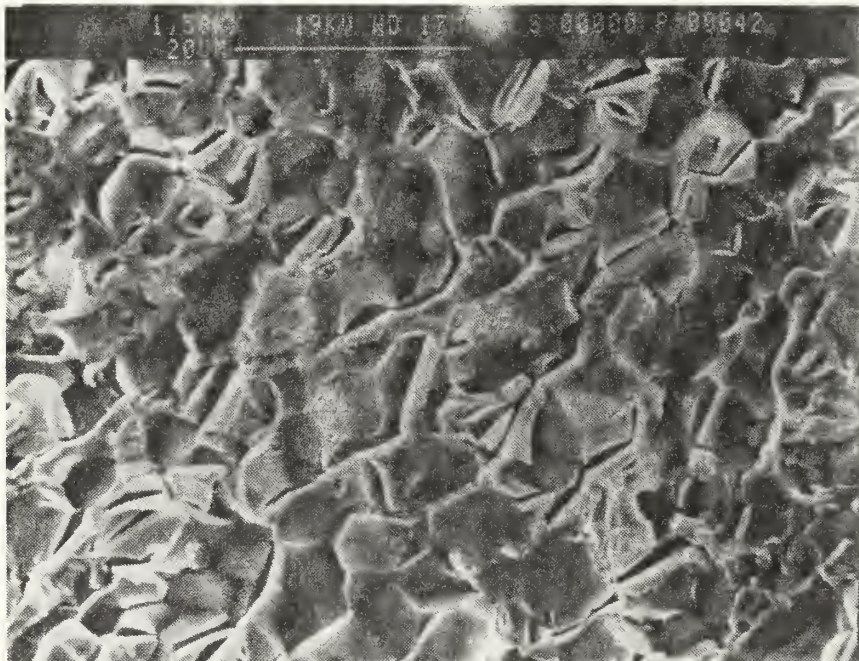


Figure 31: SEM micrograph of fracture surface of 7T sample as received, showing primarily transgranular fracture.





**Figure 32:** SEM micrograph of fracture surface of 7T sample after heat treatment at 1750°C, showing increase in microfissures and transition to intergranular fracture.



**Figure 33:** SEM micrograph of fracture surface of 7T sample after heat treatment at 1800°C, showing continued transition to intergranular fracture.



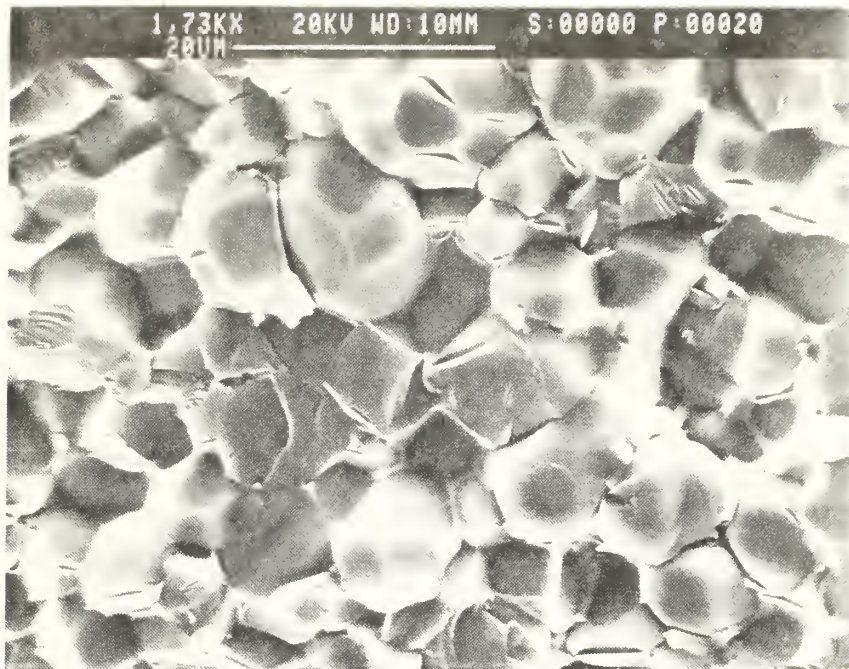


**Figure 34:** SEM micrograph of fracture surface of 7T sample after heat treatment at 1850°C, showing primarily intergranular fracture.



**Figure 35:** SEM micrograph of fracture surface of 7T sample after heat treatment at 1900°C, showing reappearance of microfissures, and primarily transgranular fracture.

is associated with a smaller  $E_b$  because of microcracks that initiate at the brittle grain boundary  $YAlO_3$ .

## 5. Transmission Electron Microscope Study

Transmission electron microscopy (TEM) reveals a low density of defects in the as-received 7C sample. Planar inversion domain boundaries (IDBs) are not evident, and the occurrence of curved IDBs is rare. Grain boundaries appear clean, i.e. with no precipitates or second phases present. Most of the second phase appears as yttrium aluminate phases at the triple points. Figure 36, shows a bright field (BF) micrograph of the sample. Energy dispersive X-ray analysis (EDX), of the yttrium aluminate phases reveals the presence of aluminum, yttrium, and oxygen. Typical X-ray spectra of these phases are shown in Figures 37a & b. These identify the areas marked 'A' and 'B' in Figure 36. It is evident from the spectra that 'A' has a higher Y/Al ratio than 'B', discounting the presence of two different phases.

Figure 38 shows a selected area diffraction pattern for the 'A' phase. Indexing of the pattern reveals this to be monoclinic  $Al_2Y_4O_9$ . Other SADPs reveal cubic  $Y_5Al_3O_{12}$ , consistent with the X-ray analysis. The concentration of  $Al_2Y_4O_9$  is too small to detected with conventional X-ray diffraction. The majority of the spots probed reveal the  $Al_5Y_3O_{12}$  phase vice  $Al_2Y_4O_9$ .

Figure 39 shows a BF micrograph of a representative grain boundary. Some strain contrast is observed at the boundary. Hence EDX was utilized to determine the possible segregation of elements. Since  $O_2$  is a major contaminant in AlN, special

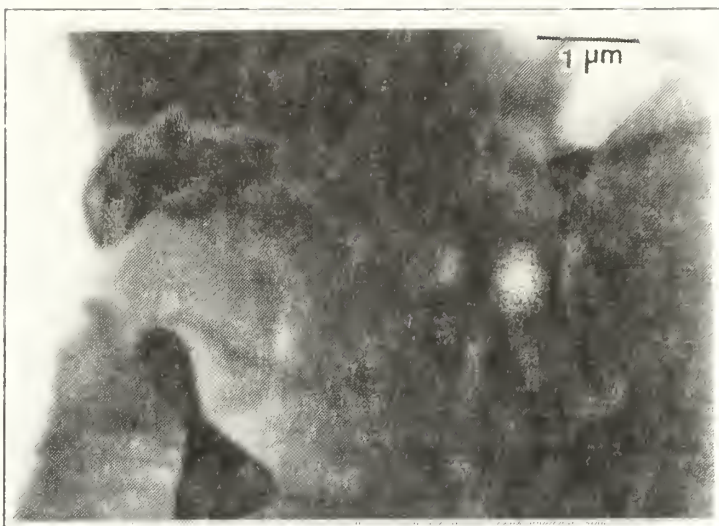


Figure 36: TEM micrograph of 7C as received, showing typical microstructure.

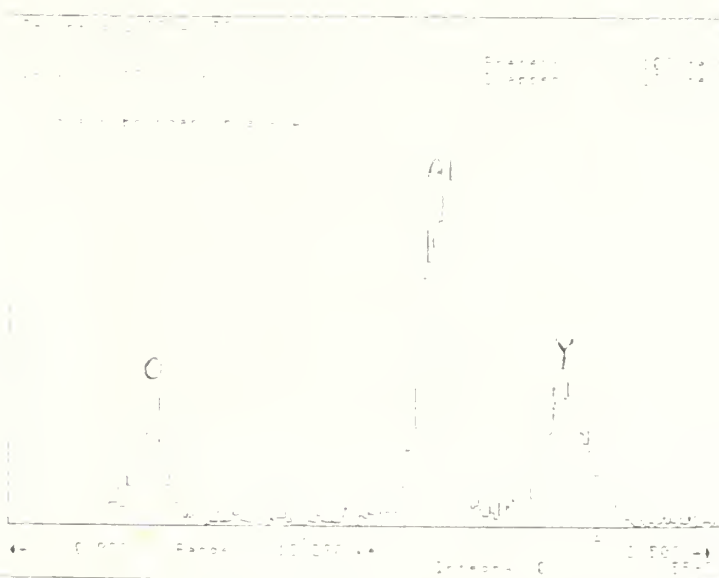


Figure 37a: Kevex X-ray spectra of region 'A' identified in Figure 36.





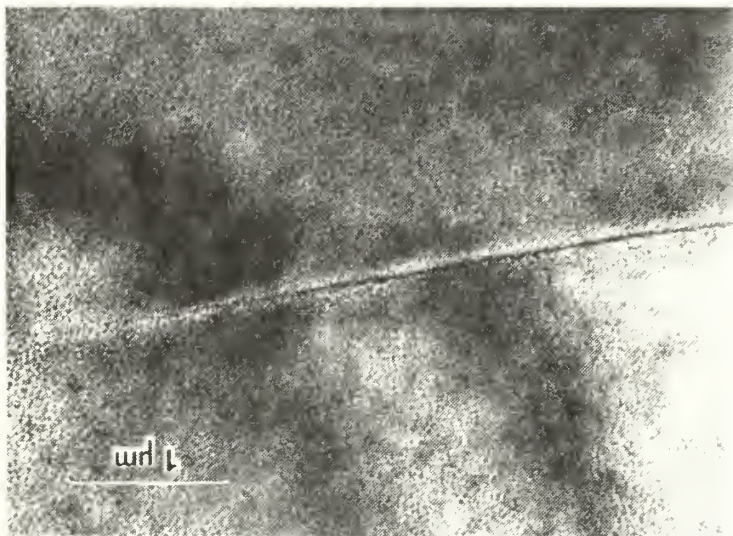


Figure 39: TEM BF micrograph of representative grain boundary.

attention is paid to the presence of oxygen at the grain boundaries. Figure 40 shows a BF micrograph of a grain boundary with three regions identified as 'A', 'B', and 'C'. X-ray EDX from these regions are shown in Figure 41a, b, and c. A careful inspection of the spectra shows an increased O<sub>2</sub> content at the boundary away from the Al<sub>5</sub>Y<sub>3</sub>O<sub>12</sub> phase. This indicates that the yttrium aluminate phase tends to gather the O<sub>2</sub> from the grain boundaries into the second phase at the triple points. Inspection of a large number of aluminate phases failed to reveal any 2-phase region.

Figure 42 shows a BF micrograph of a triple grain point in 7C sample that was heat treated at 1850°C for 7 hours in flowing dry N<sub>2</sub> atmosphere. Two distinct regions are now visible in the grain boundary phase. X-ray EDX scans of regions 'A' and 'B' are shown in Figure 43a and b. Al, O, and Y peaks were present indicating an yttrium aluminate phase at the triple grain junction marked 'A'. EDX from further along the boundary at 'B' reveals only Al and O (Figure 43b), indicating the possible evaporation/sublimation of Y<sub>2</sub>O<sub>3</sub> from this region. A more likely mechanism would involve the formation of a two-phase Liquid + Al<sub>5</sub>Y<sub>3</sub>O<sub>12</sub> mixture (Figure 13), and the loss of the Al<sub>5</sub>Y<sub>3</sub>O<sub>12</sub> phase during this liquid phase sintering step. To check this hypothesis, SADP from the aluminate phase was taken. Due to the small size, exact pole positions could not be achieved but the cubic phase was identified. Two cubic aluminate phases were obtained from the XRD analysis namely AlYO<sub>3</sub> and Al<sub>5</sub>Y<sub>3</sub>O<sub>12</sub>, which are both body-centered cubic with lattice parameters of ~12Å [Ref.26,27]. The TEM results at this stage, are thus not conclusive in identifying the aluminate phases still present after seven hours at 1850°C. Figure 44 shows a BF micrograph of a triple point

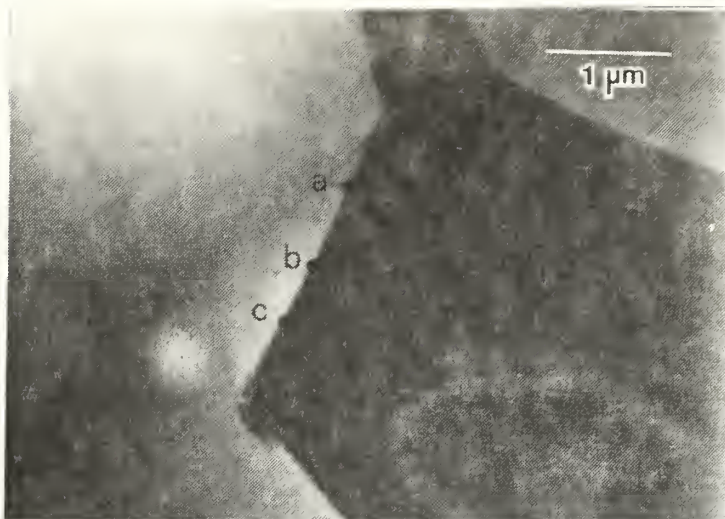


Figure 40: TEM BF micrograph with regions identified for X-ray EDX.

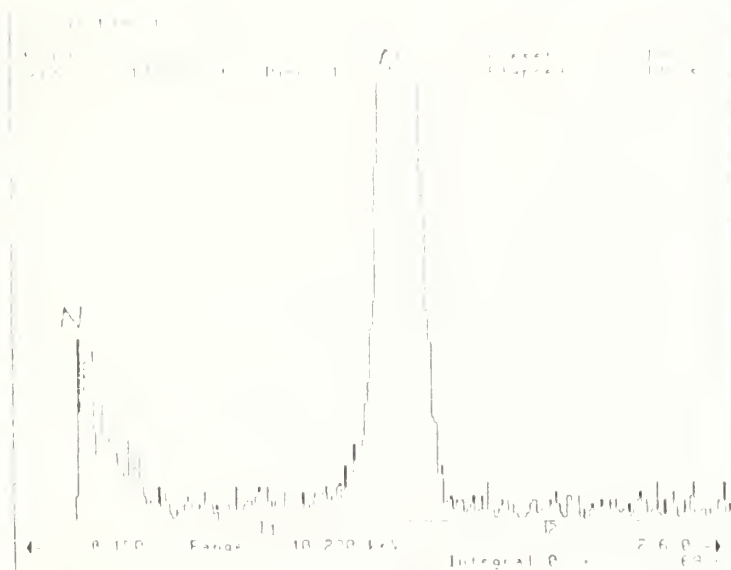


Figure 41a: X-ray EDX of region 'A' identified in Figure 40.

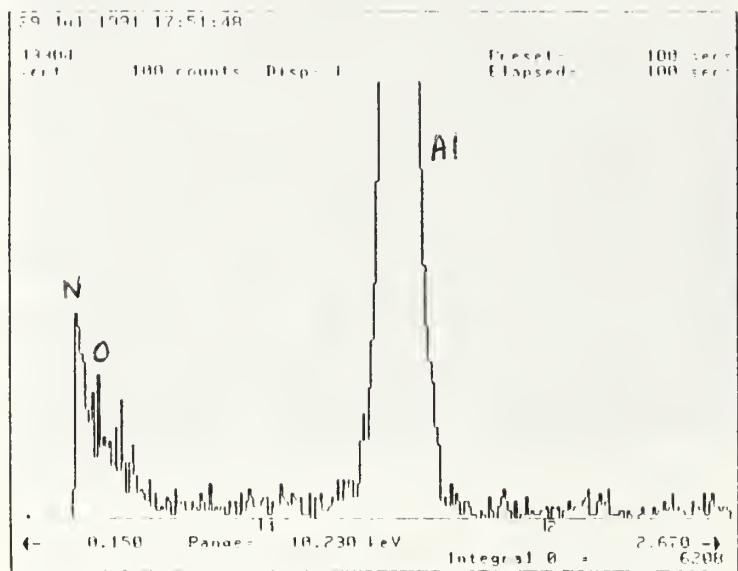


Figure 41b: X-ray EDX of region 'B' identified in Figure 40.

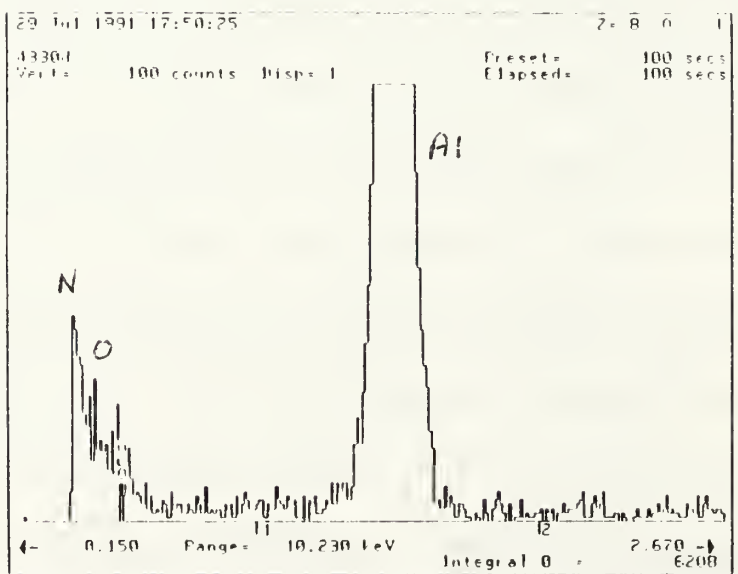


Figure 41c: X-ray EDX of region 'C' identified in Figure 40.





Figure 42: TEM BF micrograph of triple grain junction. Regions marked for EDX identification.

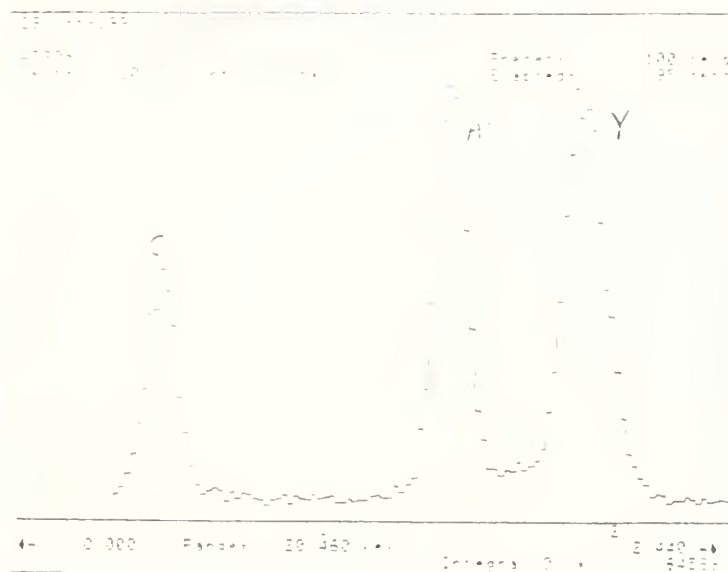


Figure 43a: Kevex EDX of region 'A' identified in Figure 42, found to contain Y, Al

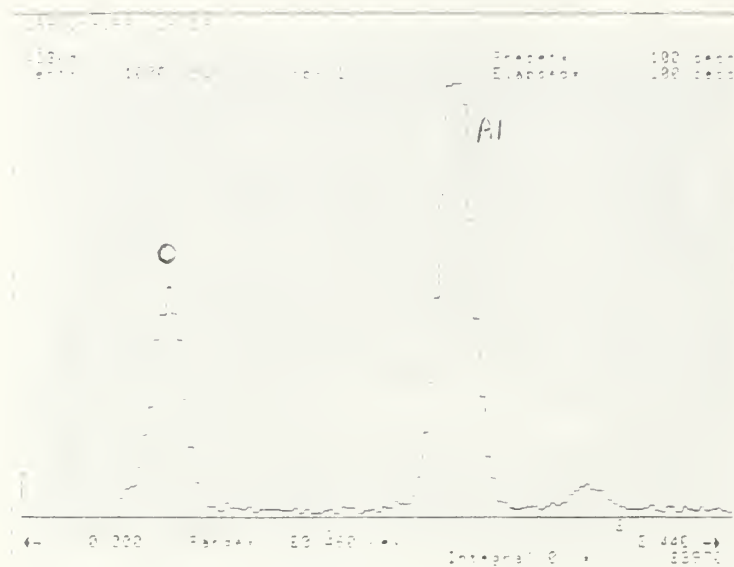


Figure 43b: Kevex EDX of region 'B' identified in Figure 42, found to contain only Al and O.

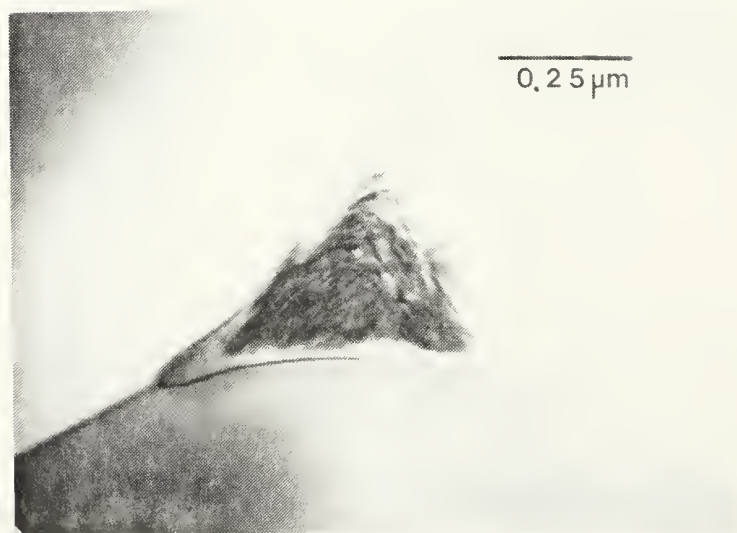
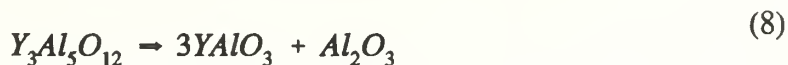


Figure 44: BF TEM micrograph of triple grain junction.

in the same sample which when probed with EDX revealed only Al and O. An SADP is shown in Figure 45. This is indexed to show the [110] zone axis of FCC  $\gamma$ - $\text{Al}_2\text{O}_3$ . The likely mechanism that could result in this grain boundary phase is the continued evaporation of  $\text{Al}_5\text{Y}_3\text{O}_{12}$  (as indicated by XRD analysis) and subsequent sintering of the remaining AlN to leave behind the  $\text{Al}_2\text{O}_3$  phase only.

It is interesting to note that the as-received AlN 7C did not show any two phase regions at the triple grain junctions, and XRD identified only the  $\text{Al}_5\text{Y}_3\text{O}_{12}$  phase. The  $\text{Al}_2\text{Y}_4\text{O}_9$  phase in this sample was only identified in the TEM. Sufficient number of sites in the heat treated 7C samples have not yet been investigated to conclusively state whether the  $\text{Al}_2\text{Y}_4\text{O}_9$  phase still exists after this seven hour heat treatment.

The development of the two phase regions consisting of  $\text{Al}_5\text{Y}_3\text{O}_{12}$  and  $\gamma$ - $\text{Al}_2\text{O}_3$ , is distinctly a result of the heat treatment. Since the  $\text{YAlO}_3$  phase is only detected in the XRD after heat treatment, it is possible that the cubic aluminate phase beside  $\text{Al}_2\text{O}_3$  in Figure 43a is obtained by a reaction such as:



The driving force for this reaction is not known at present, but it can definitely explain the reduction of the  $\text{Al}_5\text{Y}_3\text{O}_{12}$  phase found in the XRD analysis. The other mechanism for the reduction of the  $\text{Al}_5\text{Y}_3\text{O}_{12}$  could be evaporation, which is also a possibility with the  $\text{YAlO}_3$  phase, leaving behind the  $\text{Al}_2\text{O}_3$  seen in the TEM micrographs.

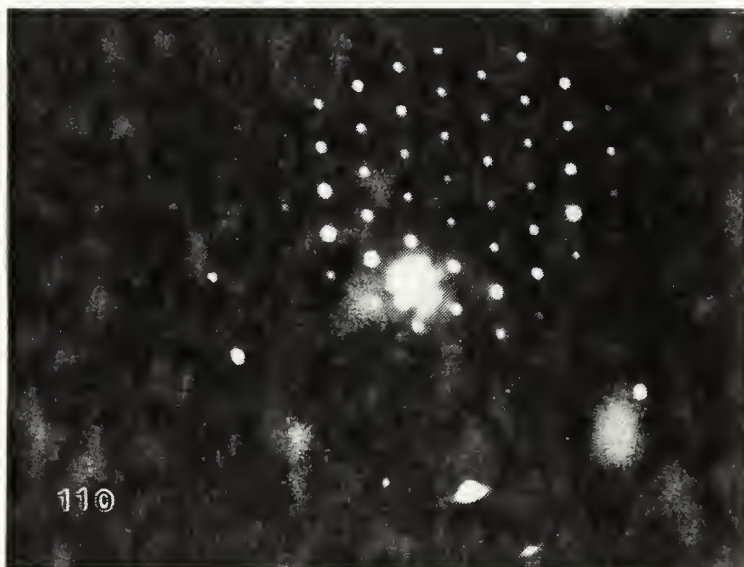


Figure 45 SADP from triple grain junction of Figure 38 revealing only presence of  $\gamma\text{-Al}_2\text{O}_3$ .



Regarding the other defects in 7C after heat treatment, the density of curved IDBs appears to increase. Figure 46 shows a BF micrograph of a curved IDB in 7C. EDX was used to investigate the O concentrations on the concave and convex sides of the IDB. No difference in the O concentrations were obtained, contrary to results obtained earlier [Ref.20].

The  $\text{YAlO}_3$  phase can be formed by quenching from above  $1060^\circ\text{C}$  [Ref.23]. After heating to  $1100^\circ\text{C}$  in  $\text{N}_2$  for two hours then quenching, TEM samples reveal the presence of a cubic yttrium aluminate phase, Figure 47. This indexed to have a [123] zone axis in the bcc structure. Since both  $\text{YAlO}_3$  and  $\text{Al}_5\text{Y}_3\text{O}_{12}$  have cubic (body centered) structures, accurate measurements of lattice parameter are required to distinguish between the two, and no such determination could be made here.  $\text{YAlO}_3$  is also seen next to  $\text{Al}_2\text{O}_3$  in the BF TEM micrograph of Figure 48, where the formation of these two phase regions ( $\text{YAlO}_3$  &  $\text{Al}_2\text{O}_3$ ), after heat treatment at relatively low temperatures ( $1100^\circ\text{C}$ ) occurs.

TEM studies of the as-received 7R sample yielded some differences from the 7C samples described above. The 7R AlN material was sintered with significantly more  $\text{Y}_2\text{O}_3$  than 7C. The BF micrograph of Figure 49 reveals a curved IDB and a second phase particle that appears to lie on the defect. Overall, the incidence of curved IDBs was more significant than in the as-received 7C samples. EDX from the regions marked 'A', 'B', 'C', and 'D' in Figure 49 are shown in Figure 50. The results indicate that the second phase particle contains yttrium, and is probably a yttrium aluminate particle.

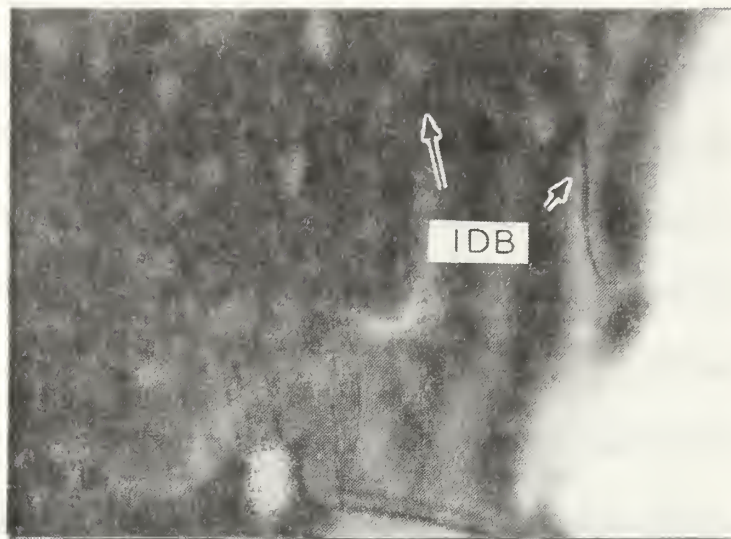


Figure 46: TEM BF micrograph of curved IDB marked for investigation of oxygen content.

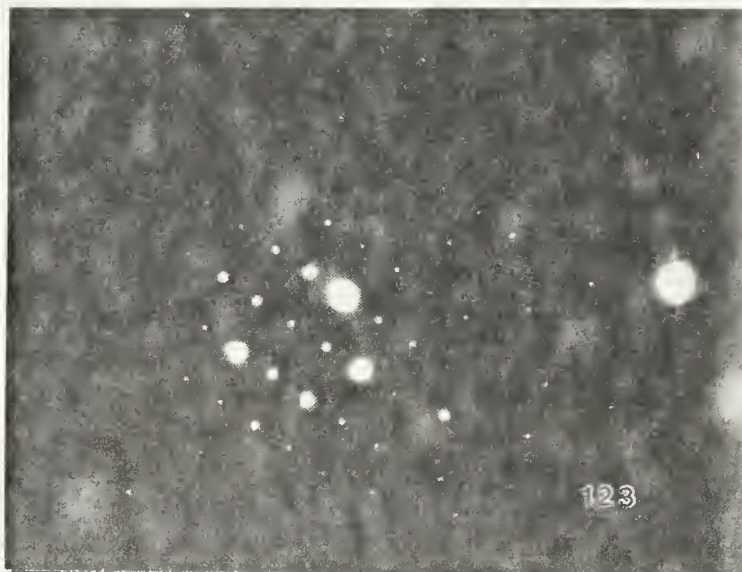


Figure 47: SADP of 7C sample quenched from 1100°C



Figure 48: TEM BF micrograph revealing two phase region of  $\text{Al}_2\text{O}_3$  and  $\text{YAlO}_3$ .

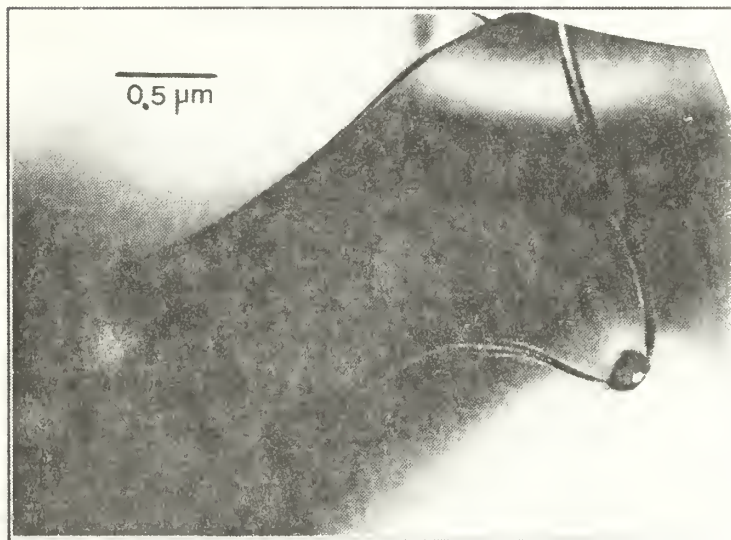
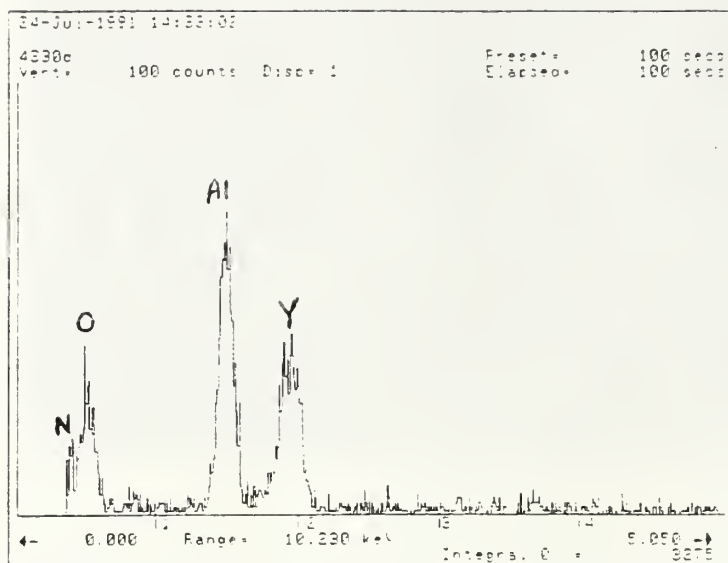
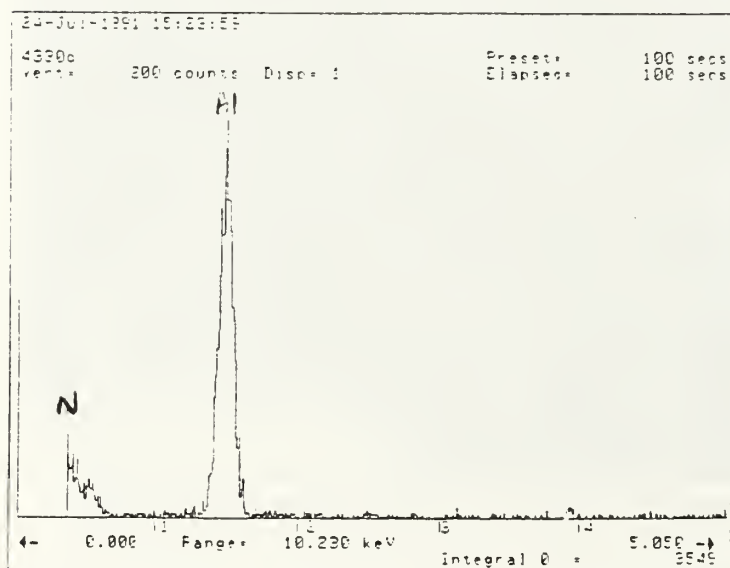


Figure 49: TEM BF micrograph of 7R revealing a curved IDB with a second phase particle lying on the defect.



**Figure 50a:** Kevex EDX of region 'A' identified in Figure 49.



**Figure 50b:** Kevex EDX of region 'B' identified in Figure 49.



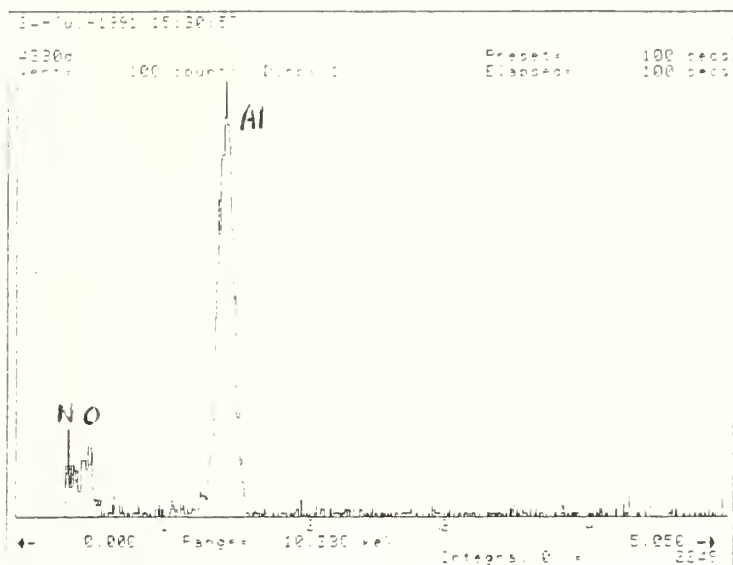


**Figure 50c:** Kevex EDX of region 'C' identified in Figure 49.

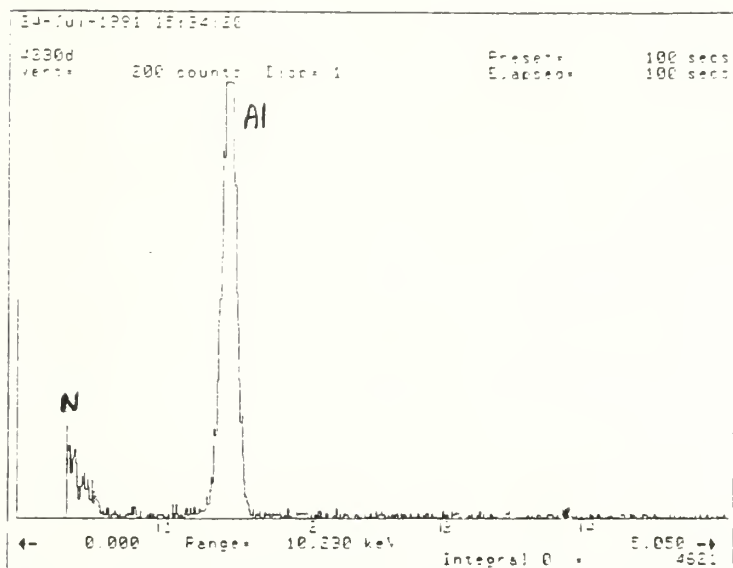


**Figure 50d:** Kevex EDX of region 'D' identified in Figure 49.

The presence of second phase Y-rich particles within AlN grains, although not specifically addressed or rationalized in the literature, has been observed. We propose that these Y-rich phases are incorporated within the AlN grains during sintering when grain boundaries migrate past small particles of these phases. It has been hypothesized by Westwood and Notis [Ref.19] that planar IDBs (not observed in the present work are formed due to boundary migration during sintering, while curved IDBs (Figure 49) are formed during powder manufacture. However, in this work, no planar IDBs were observed, suggesting that sintering does not always result in the formation of these defects. Additionally, although previous investigators have reported that curved IDBs usually have higher oxygen content than the matrix (although not as high as planar IDBs), the curved IDBs probed with a windowless EDX detector in this study did not show appreciably higher oxygen contents than the rest of the AlN matrix. Also the pinning of curved defects by Y-rich second phase particles, as observed in Figure 49, suggests that the curved defects migrate during sintering, and on encountering second phase particles, bow out around them (much like dislocations). Since these second phase particles are incorporated into the AlN grains only during sintering, the curved defects existing within the same grains as the particles must also have originated during sintering. This is in disagreement with Westwood and Notis' hypothesis that curved defects originate solely during powder manufacture.

Spot 'A', (Figure 50a), on the convex side of the curved IDB, is richer O than spot 'D' (Figure 50d), on the concave side of the IDB. The mechanism for this

type of O partitioning is not yet clearly established. It may be recalled that no such oxygen partitioning was observed in the vicinity of curved IDBs in the 7C sample.

Figure 51, shows a BF micrograph of the general microstructure in 7R. The yttrium aluminate phases appear to be concentrated in regions that appear almost as large as the AlN grains themselves. Very little triple grain junction second phase appears. This duplicates what is seen in the SEM micrograph of the 7R sample (Figure 12). Figure 52 shows another second phase (yttrium containing) particle inside the AlN grain with misfit dislocations. Another type of defect, the 'D' shaped defect often seen in AlN, is also present in 7R. Figure 53, shows a BF micrograph of a 'D' shaped defect with one planar IDB, and a curved IDB. These defects were more common in the 7R samples.

An unusual phenomenon was observed in the diffraction patterns on the exact [0001] pole orientation for both the 7R and 7C samples in the TEM study. Extra spots or 'satellite' spots appear around the  $10\bar{1}0$  and  $2\bar{1}\bar{1}0$  spots of AlN in Figure 54. This effect can be explained by double diffraction from an overlay of  $\alpha\text{-Al}_2\text{O}_3$  (rhombohedral structure), on the [0001] planes of AlN, with the c-axis of the rhombohedral structure parallel to the c-axis of AlN. To investigate whether it is a surface or bulk phenomenon, a sample was prepared by milling in liquid nitrogen (as usual), and transferred to the TEM immediately. A SADP of the [0001] pole is shown in Figure 55. This shows a much reduced satellite effect around the diffraction spots.

Aging in laboratory air at 75°C for 15 hours produced the SADP shown in Figure 56, and the BF image in Figure 57. The satellite spots and the features observed



Figure 51: TEM BF micrograph showing typical microstructure of AlN 7R.

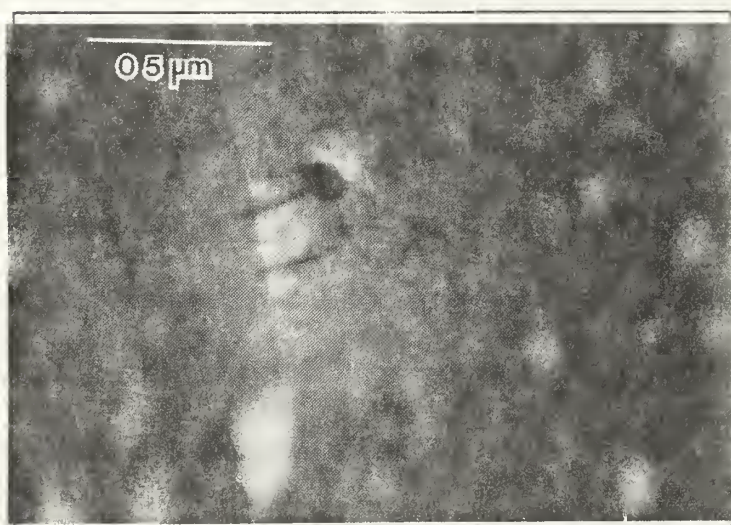


Figure 52: TEM BF micrograph of 7R sample showing yttrium containing particle with AlN grain.



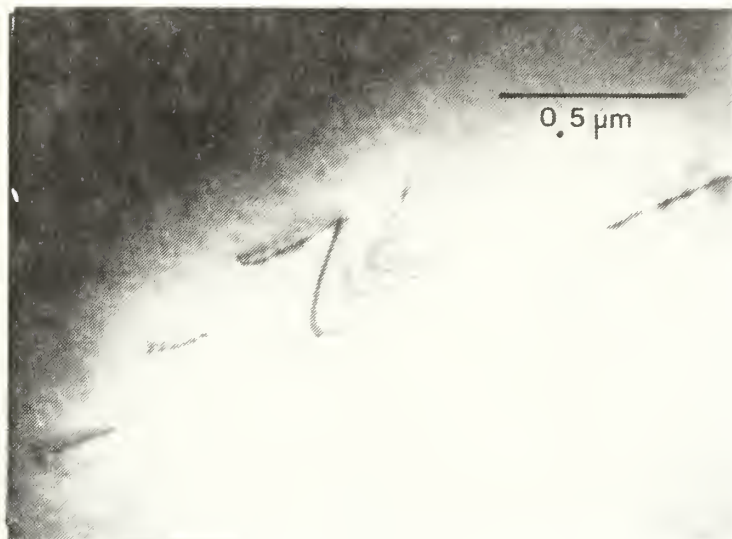


Figure 53: TEM BF micrograph of 7R showing a 'D' shaped defect within the AlN grain from the intersection of a planar and curved IDB.

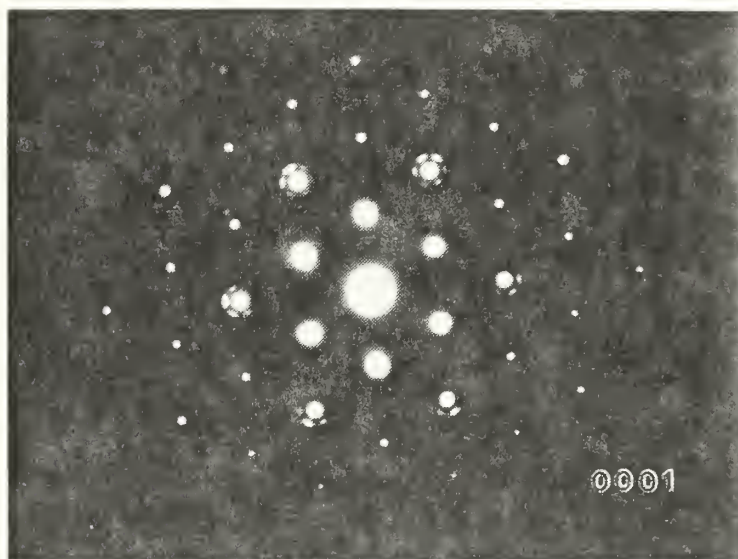
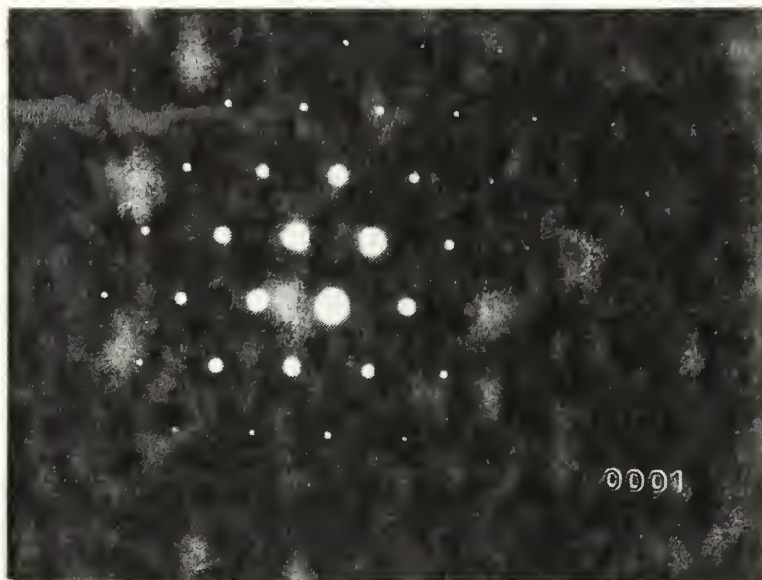
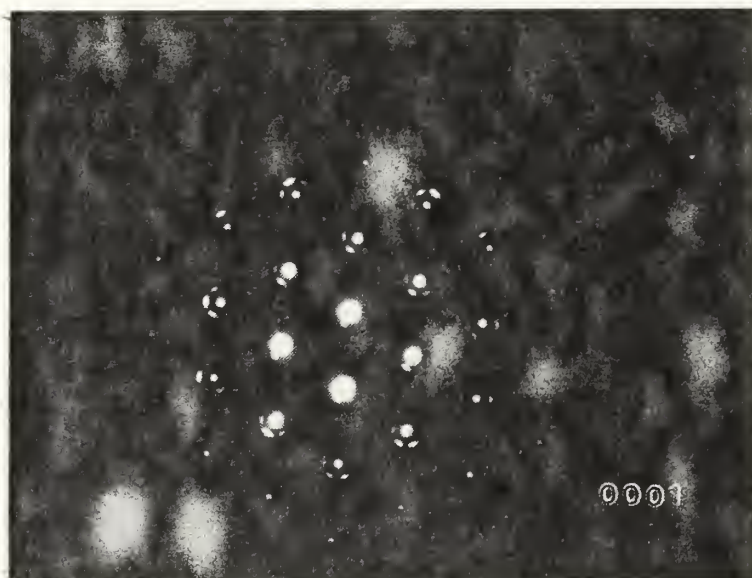


Figure 54: SADP of AlN grain with extra spots around 1010 and 2110 spots due to double diffraction by Al<sub>2</sub>O<sub>3</sub>.



**Figure 55:** SADP of sample from Figure 54 immediately after ion milling showing reduction of satellite spots.



**Figure 56:** SADP of AlN sample of Figures 54 and 55 after aging at 75°C for 15 hours in laboratory air showing increase in satellite spots.

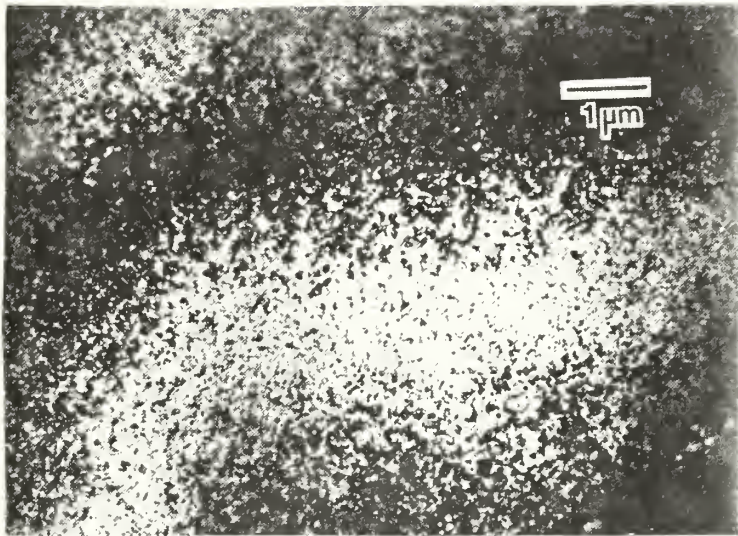


Figure 57: TEM BF micrograph of sample from Figure 56 showing coarse surface after aging.

in the BF image seem to have intensified. This could be due to an enhanced surface oxide, or due to an internal precipitate. The same sample was then milled again in liquid nitrogen to remove any surface layer and examined immediately. The satellite features are reduced significantly but still visible. This strongly indicates that the features are associated with a surface phenomenon.

Other poles were observed to investigate the orientation relationship between the oxide and AlN. Figure 58 shows a  $(11\bar{2}3)$  pole of AlN with no satellites present. Another feature is however evident, namely a ring superimposed on the  $[11\bar{2}3]$  AlN pattern. This ring pattern is indexed to give  $\gamma$ -Al<sub>2</sub>O<sub>3</sub> (cubic). It can be concluded from the evidence presented, that an Al<sub>2</sub>O<sub>3</sub> oxide forms instantaneously on fresh surfaces of AlN. When the grain orientation is near  $[0001]$  at the surface,  $\alpha$ -Al<sub>2</sub>O<sub>3</sub> (rhombohedral) forms with an epitaxial relationship. If the exposed surface is appreciably removed from  $[0001]$ , a polycrystalline  $\gamma$ -Al<sub>2</sub>O<sub>3</sub> forms instead of the epitaxial  $\alpha$ -Al<sub>2</sub>O<sub>3</sub>. These results could be significant in the metalization and coating of AlN substrates, where depositions made on 'clean' AlN substrates might have small regions of epitaxial oxide already present.





**Figure 58:** SADP of  $[11\bar{2}3]$  pole of AlN, no satellites present.

#### IV. CONCLUDING REMARKS

AlN samples sintered with different amounts of  $Y_2O_3$  in the starting powder were studied with respect to their phase constitution and properties after heat treatment at 1750°C, 1800°C, 1850°C and 1900°C.

At low  $Y_2O_3$  additions (1.77 wt. %), only  $Al_5Y_3O_{12}$  was found (in addition to AlN) in the as-received state. On heat treatment at 1750°C for 2 hours, non-equilibrium  $YAlO_3$  (cubic) formed, which together with  $Al_5Y_3O_{12}$  gradually disappeared with heat treatment at progressively higher temperatures. Concurrent with these phase changes, the fracture properties were found to vary considerably. In the following, a mechanism is proposed to correlate the failure mode to the processes occurring during sintering.

Upon formation of  $YAlO_3$ , the fracture mode changed from primarily intergranular to transgranular, with the appearance of numerous microfissures, indicating that this phase contributes to microcrack nucleation. Although most of these microcracks are stopped on entering the AlN grains, some of them aid in cleavage.

With increasing heat treatment temperature, up to 1850°C, the grain boundary phases start evaporating, although the sintering processes are not quick enough to seal the resulting pores. This results in a progressively larger intergranular component to fracture. At 1900°C, however, sintering is rapid, and this results in considerable sealing of pores left by evaporation, causing the reversal to transgranular fracture.

At high  $Y_2O_3$  contents (3.79 and 4.23 wt. %),  $Al_5Y_3O_{12}$  and the metastable  $AlYO_3$  (orthorhombic) were present in the as-received state. The amount of  $AlYO_3$  diminished with heat treatment at temperatures up to  $1850^\circ C$ , beyond which it increased. The amount of  $Al_5Y_3O_{12}$ , however, decreased from the very start. Once again, this was associated with a change in the failure modes (in 3-point bending). In the following we propose a mechanism to explain the observed trends. With increased temperature of heat treatment, the fracture becomes more intergranular while losing  $AlYO_3$  and  $Al_5Y_3O_{12}$  and showing a decrease in  $E_b$ . These samples had a large fraction of second phase aluminates in the as-received state and heat treatment up to temperatures less than  $1850^\circ C$  did not lead to any liquefaction. The continuous loss of the aluminate phases is faster than the sintering effect of the AlN grains leading to early intergranular fracture and a concurrent drop in  $E_b$ . Above  $1850^\circ C$ , the formation of liquid phases occurs and leads to LPS and improved  $E_b$  values. The fracture mode becomes more transgranular in nature (compared to the as-received sample) and is due to the improved LPS that occurs at this stage.

On comparing the two materials (low and high  $Y_2O_3$  content), it is clear that the amount of the grain boundary phase affects the fracture behavior of the heat treated material. When the aluminate phases are abundant enough, heat treatment below  $1850^\circ C$  gave a decrease in  $E_b$  and an increase in the intergranular nature. When the aluminates are not as abundant, the mechanical properties depend more strongly on the type of phases formed during the heat treatment.

From the above, it is clear that the second phase constitution affects the mechanical properties of the sintered AlN greatly. Accordingly, the physical properties, eg.

coefficient thermal expansion and thermal conductivity, are also expected to vary appreciably with heat treatment, and will be studied in follow-on work.

Also, it is apparent that although both the low  $\text{Y}_2\text{O}_3$  content material (7C) and the high  $\text{Y}_2\text{O}_3$  content material (7R and 7T) were subjected to identical heat treatment schedules after initial sintering, different metastable phases were formed in these materials.  $\text{YAlO}_3$  (cubic) formed at low  $\text{Y}_2\text{O}_3$ , while  $\text{AlYO}_3$  (orthorhombic) formed at high  $\text{Y}_2\text{O}_3$ . Although it is plausible that this may be the effect of the initial sintering temperature, it is unlikely for the following reason. Both 7C and 7T (1.77 wt. % and 4.23 wt. %, respectively) were sintered at liquid phase sintering temperatures, while 7R (3.79 wt. %) was sintered at temperatures below that required for liquefaction of the additives. Yet, 7C had only  $\text{Al}_5\text{Y}_3\text{O}_{12}$  to begin with and formed  $\text{YAlO}_3$  after heat treatment at  $1750^\circ\text{C}$ , while 7R and 7T contained  $\text{AlYO}_3$  and  $\text{Al}_5\text{Y}_3\text{O}_{12}$ . This strongly suggests that the formation of orthorhombic  $\text{AlYO}_3$  is favored at high  $\text{Y}_2\text{O}_3$  contents, while cubic  $\text{YAlO}_3$  is formed at low  $\text{Y}_2\text{O}_3$  contents. Thus, the amount of  $\text{Y}_2\text{O}_3$  addition is the primary factor in determining which metastable phase is formed.

The TEM study showed a greater concentration of curved IDBs in the high  $\text{Y}_2\text{O}_3$  containing material, although planar IDBs were absent. IDBs have been shown to represent a boundary across which the bonding changes from Al-N to Al-Al or N-N and has, in the case of planar IDBs, been associated with an increased oxygen content. The curved IDBs seen here did not show a concentration of oxygen on the defect, and the few such curved defects probed in the low  $\text{Y}_2\text{O}_3$  containing material showed no distinguishable difference in oxygen content on the convex and concave sides. In the



higher  $\text{Y}_2\text{O}_3$  containing material, the curved IDBs showed a discernible difference in oxygen concentration on both sides of the defect. No model for the curved IDB defects exists to date, and the reason for the variation in  $\text{O}_2$  content across the IDB is not clear at present.

With respect to the grain boundary phases, after heat treatment at  $1850^\circ\text{C}$ , the low  $\text{Y}_2\text{O}_3$  containing material showed the presence of 2 phase regions concurrent with the XRD results. A large fraction of the grain boundary phases was found to contain only  $\gamma\text{-Al}_2\text{O}_3$  exactly at the triple grain points. No such regions were found in the as-received samples, suggesting that evaporation loss of the Y containing phases does occur during heat treatment.

Finally, the surface of AlN was found to be very sensitive to oxidation. Epitaxial growth of  $\alpha\text{-Al}_2\text{O}_3$  were observed to form on freshly cleaned surfaces of AlN grains with the (0001) planes exposed. The epitaxial oxide was spotty (rather than continuous). A plausible explanation for this phenomenon is that the oxide forms only in regions where Al atoms (and not N) are exposed to the surface.

## LIST OF REFERENCES

1. Iwase, N., Anzai, K., and Shinozaki, K., "Aluminum Nitride Substrates Having High Thermal Conductivity," *Solid State Technology*, pp. 135-138, October, 1986.
2. Prohaska, G., and Miller, G., "Aluminum Nitride: A Review of the Knowledge Base for Physical Property Development," *Mat. Res. Soc. Symp.*, Vol. 167, pp. 215-227, 1990.
3. Chanchani, R., "Processibility of Thin-Film, Fine-Line Pattern on Aluminum Nitride Substrates for HIC's," *IEEE Trans. Comp., Hybrids, Manuf. Technol.*, Vol. 8, pp. 584-588, 1988.
4. Westwood, A., and Notis, M., "Metallization Issues in Advances Ceramic Substrates:- Microstructural, Microchemistry, and Thermal Conductivity in AlN," *Mat. Res. Soc. Symp. Proc.*, Vol. 154, pp. 479-485, 1989.
5. Virkar, A., Jackson, T., and Cutler, R., *J. Am. Ceram. Soc.*, Vol. 72, pp. 203-109, 1989.
6. Anzai, K., Iwase, N., Shinzaki, K., and Tsuge, A., "Development of High Thermal Conductivity Aluminum Nitride Substrate Material by Pressureless Sintering," *Proceeding of the 1st IEEE CHMT Symposium, Tokyo*, pp. 23-28, 1984.
7. Kurokawa, Y., Hamaguchi, H., Shimada, Y., Utsumi, K., Takamizawa, H., Kamata, T., Noguchi, S., "Development of Highly Thermal Conductive AlN Substrate by Green Sheet Technology," *Proceedings of the 36th Electronic Components Conference*, pp. 412-418, 1986.
8. Slack, G. and McNelly, T., "AlN Single Crystals," *Journal of Crystal Growth*, Vol. 42, pp. 560-563, 1977.
9. Slack, G., "Nonmetallic Crystals with High Thermal Conductivity," *J. Phys. Chem. Solids*, Vol. 34, pp. 321-335, 1973.
10. Kurokawa, Y., Utsumi, K., Takamizawa, H., "Development and Microstructural Characterization of High-Thermal-Conductivity Aluminum Nitride Ceramics," *J. Am. Ceram. Soc.*, Vol. 71, No. 7, pp. 588-94, 1988.

11. Troczynski, T., and Nicholson, P., "Effect of Additives on the Pressureless Sintering of Aluminum Nitride between 1500° and 1800°C," *J. Am. Ceram. Soc.*, Vol. 72, No. 8, pp. 1488-91, 1989.
12. Enloe, J., Rice, R., Lau, J., Kumar, R., Lee, S., "Microstructural Effects of the Thermal Conductivity of Polycrystalline Aluminum Nitride," *J. Amer. Ceram., Soc.*, Vol. 74, No. 8, pp. 2214-19, 1991.
13. Harris, J. H., Youngman, R. A., and Teller, R. G., "On the Nature of the Oxygen-Related Defect in Aluminum Nitride," *Journal of Materials Research Society*, Vol. 5, No. 8, pp. 1763-72, 1990.
14. Horvath, S., Witek, S. and Harmer, M., "Effects of Carbon and Calcium Oxide on the Sintering Behavior of Aluminum Nitride," *Proceedings of the Int. Symposium on Ceramic Substrates and Packages, Sponsored by the Elec. Div. of the Amer. Cer. Soc. and the Cer. Soc. of Japan, held in Denver, CO, on October 18-21, 1987*, pp. 121-132, 1987.
15. Lenel, F., *Powder Metallurgy Principles and Applications*, pp. 285-307, Metal Powder Industries Federation, 1980.
16. Takashi, T., Iwase, N., and Nagata, M., "Properties and Reliability of AlN Ceramics for Power Devices," *Proceedings of the Int. Symposium on Ceramic Substrates and Packages, Sponsered by the Elec. Div. of the Amer. Cer. Soc. and the Cer. Soc. of Japan, held in Denver, CO, on October 18-21, 1987*, pp. 159-169, 1987.
17. Marchant, D. D., and Nemecek, T. E., "Aluminum Nitride: Preparation, Processing, and Properties," *Proceedings of the Int. Symposium on Ceramic Substrates and Packages, Sponsered by the Elec. Div. of the Amer. Cer. Soc. and the Cer. Soc. of Japan, held in Denver, CO, on October 18-21, 1987*, pp. 19-54, 1987.
18. Kuramoto, M., Taniguchi, H., Numata, Y., Aso, I., "Sintering Process of Translucent AlN and Effect of Impurities on Thermal Conductivity of AlN Ceramics," *Yogyo-Kyokai-Shi*, Vol. 93,. No. 9, pp. 517-22, 1985.
19. Westwood, A., and Notis, M., "Planar and Curved Defects in Aluminum Nitride: Their Microstructure and Microchemistry," *Mat. Res. Soc. Symp. Proc.*, Vol. 167, pp. 265-70, 1990.
20. Youngman, R., Harris, J., Labun, P., Graham, R., and Weiss, J., "Inversion Domain Boundaries and Oxygen Accommodation in Aluminum Nitride," *Mat. Res. Soc. Symp. Proc.*, Vol. 167, pp. 271-6, 1990.

21. Harris, J. and Youngman, R, "Time-Resolved Luminescence of Oxygen Related Defects in Aluminum Nitride," *Mat. Res. Soc. Symp. Proc.*, Vol. 167, pp. 253-8, 1990.
22. McKernan, S., and Carter, C., "On the Structure of Planar Defects in AlN," *Mat. Res. Soc. Symp. Proc.*, Vol. 167, pp. 259-264, 1990.
23. Yamaguchi, O., Matui, K., and Shimizu, K., *Ceram, Inc.*, Vol. 107, 1985.
24. Levin, E., Robbins, C., and McMurdie, H., *Phase Diagrams for Ceramists, 1969 Supplement*, Reser, M.,ed., p. 96, The American Ceramic Society, 1969.
25. Weast, R. ed., *CRC Handbook of Chemistry and Physics, 53rd Edition*, p. B-153, CRC Press, 1972.
26. National Bureau of Standards. (U. S.), Mono. Gr. 25, Sec. 19, 1982.



## INITIAL DISTRIBUTION LIST

	No. Copies
1. Defense Technical Information Center Cameron Station Alexandria, VA 22304-6145	2
2. Library, Code 52 Naval Postgraduate School Monterey, CA 93943-5002	2
3. Department Chairman, Code ME/HY Department of Mechanical Engineering Naval Postgraduate School Monterey, CA 93943-5000	1
4. Professor I. Dutta, Code ME/DU Department of Mechanical Engineering Naval Postgraduate School Monterey, CA 93943-5000	2
5. Professor S. Mitra, Code ME/MT Department of Mechanical Engineering Naval Postgraduate School Monterey, CA 93943-5000	2
6. Professor B. Neta, Code MA/NE Department of Mathematics Naval Postgraduate School Monterey, CA 93943-5000	1
7. LT John H. Cooper 111 Cooper Road Pauline, SC 29374-9517	1
8. Naval Engineering Curricular Office, Code 34 Naval Postgraduate School Monterey, CA 93943-5000	1

- |      |  |   |
|------|--|---|
| 9.   | <b>Professor K. Spear</b><br><b>Department Chairman, Ceramic Science and Engineering</b><br><b>College of Earth and Mineral Sciences</b><br><b>University Park, PA 16802</b> | 1 |
| <br> |  |   |
| 10.  | <b>J. Wolford, Code 6051</b><br><b>Branch Manager, Advanced Packaging</b><br><b>Naval Weapons Support Center</b><br><b>Crane, IN 47522</b>                                   | 1 |







Thesis

C754043 Cooper

c.1

Process-dependence of  
properties in high ther-  
mal conductivity alu-  
minum nitride substrates  
for electronic packaging.

Thesis

C754043 Cooper

c.1

Process-dependence of  
properties in high ther-  
mal conductivity alu-  
minum nitride substrates  
for electronic packaging.



DUDLEY KNOX LIBRARY



3 2768 00034099 6